© 2023. Published by The Company of Biologists Ltd | Journal of Cell Science (2023) 136, jcs260474. doi:10.1242/jcs.260474

RESEARCH ARTICLE

SPECIAL ISSUE: CELL BIOLOGY OF MOTORS

The kinesin-5 protein Cut7 moves bidirectionally on fission yeast spindles with activity that increases in anaphase

Zachary R. Gergely[1,2], Saad Ansari[1], Michele H. Jones[1,2], Bojun Zhou[1], Cai Cash[1], Richard McIntosh[2] and Meredith D. Betterton[1,2,3,*]

ABSTRACT

Kinesin-5 motors are essential to separate mitotic spindle poles and assemble a bipolar spindle in many organisms. These motors crosslink and slide apart antiparallel microtubules via microtubule plus-end-directed motility. However, kinesin-5 localization is enhanced away from antiparallel overlaps. Increasing evidence suggests this localization occurs due to bidirectional motility or trafficking. The purified fission-yeast kinesin-5 protein Cut7 moves bidirectionally, but bidirectionality has not been shown in cells, and the function of the minus-end-directed movement is unknown. Here, we characterized the motility of Cut7 on bipolar and monopolar spindles and observed movement toward both plus- and minus-ends of microtubules. Notably, the activity of the motor increased at anaphase B onset. Perturbations to microtubule dynamics only modestly changed Cut7 movement, whereas Cut7 mutation reduced movement. These results suggest that the directed motility of Cut7 contributes to the movement of the motor. Comparison of the Cut7 mutant and human Eg5 (also known as KIF11) localization suggest a new hypothesis for the function of minus-end-directed motility and spindle-pole localization of kinesin-5s.

KEY WORDS: Mitosis, Kinesin-5, Cut7, Bidirectional movement, Eg5, Fission yeast

INTRODUCTION

Although kinesin-5 motors have long been known to play an important role in bipolar mitotic spindle assembly and chromosome segregation, the links between kinesin-5 motility, localization and force generation remain incompletely understood. Kinesin-5 motors are essential for mitotic spindle formation in many organisms because they separate spindle poles to build a bipolar spindle (Enos and Morris, 1990; Hagan and Yanagida, 1990; Hoyt et al., 1992; Sawin et al., 1992; Blangy et al., 1995; Fig. 1). Kinesin-5s are homo-tetramers, with two dimeric motors linked antiparallel by a central minifilament (Cole et al., 1994; Kashina et al., 1996; Gordon and Roof, 1999; Acar et al., 2013; Scholey et al., 2014; Singh et al., 2018; Fig. 1A,B). Thus, kinesin-5 proteins can crosslink antiparallel microtubules (MTs) and slide them apart, both in cells and in reconstituted systems (Sharp et al., 1999; Kapitein et al., 2005; Hildebrandt et al., 2006; Tao et al., 2006; van den Wildenberg et al., 2008; Shimamoto et al., 2015; Bodrug et al., 2020). This activity contributes both to spindle pole separation as the bipolar spindle forms and to spindle elongation in anaphase B (Goshima and Scholey, 2010; Mann and Wadsworth, 2018; Scholey et al., 2016). Antiparallel sliding is therefore crucial to kinesin-5 function in mitosis and depends on the motility of the motor toward MT plus-ends (Fig. 1C). Consistent with this view, kinesin-5 depletion or inhibition leads to monopolar spindles (Hagan and Yanagida, 1990; Sawin et al., 1992; Mayer et al., 1999).

However, more recent results have called into question whether the elegantly simple antiparallel-sliding model can fully explain kinesin-5 function. Antiparallel sliding requires antiparallel MTs, which are most abundant near the center of the spindle, where MTs from both poles interdigitate (McIntosh and Landis, 1971; Ding et al., 1993). However, kinesin-5s localize more strongly near spindle poles in many organisms (Fig. 1), including *Schizosaccharomyces pombe* (Hagan and Yanagida, 1992), *Saccharomyces cerevisiae* (Shapira et al., 2017), *Xenopus laevis* (Sawin et al., 1992; Cahu et al., 2008) and mammalian (Blangy et al., 1995; Gable et al., 2012) cells. We have limited understanding of how pole localization occurs for a plus-end-directed motor, but there are three broad ideas for the mechanism: trafficking by a minus-end-directed motor that carries kinesin-5 as cargo, an intrinsic bidirectional motility of kinesin-5 that moves motors toward spindle poles, and direct pole binding.

Minus-end-directed trafficking occurs for the vertebrate kinesin-5 Eg5 (also known as KIF11), which is plus-end-directed but can be transported toward MT minus-ends by dynein (Uteng et al., 2008; Gable et al., 2012) The trafficking is regulated by TPX2 (Ma et al., 2010, 2011; Gable et al., 2012; Balchand et al., 2015). Importantly, chimeric kinesin-5s made from the Eg5 tail and the motor of other kinesins fail to assemble a bipolar spindle, even though these motors localize to spindle MTs (Cahu and Surrey, 2009). This evidence suggests that bidirectional trafficking of Eg5 by dynein might play a role in spindle assembly.

Both budding and fission yeast kinesin-5s have intrinsic bidirectional motility on MTs *in vitro* (Roostalu et al., 2011; Gerson-Gurwitz et al., 2011; Avunie-Masala et al., 2011; Thiede et al., 2012; Fridman et al., 2013; Edamatsu, 2014, 2016; Britto et al., 2016). For budding-yeast kinesin-5 protein Cin8, the average direction of motion changes with solution conditions and mutations (Gerson-Gurwitz et al., 2011; Roostalu et al., 2011; Shapira and Gheber, 2016; Shapira et al., 2017). Other work suggests that crowding on the MT lattice and motor clustering affect kinesin-5 speed and directionality (Britto et al., 2016; Shapira et al., 2017; Bodrug et al., 2020).

The kinesin-5 C-terminal tail contributes to spindle and spindle-pole localization. The tail contains conserved phosphorylation sites (Heck et al., 1993; Sawin and Mitchison, 1995; Blangy et al., 1995; Drummond and Hagan, 1998; Cahu et al., 2008; Rapley et al., 2008;

[1]Department of Physics, University of Colorado Boulder, Boulder, CO 80305, USA. [2]Department of Molecular, Cellular, and Developmental Biology, University of Colorado Boulder, Boulder, CO 80305, USA. [3]Center for Computational Biology, Flatiron Institute, New York, NY 10010, USA.

*Author for correspondence (mdb@colorado.edu)

M.D.B., 0000-0002-5430-5518

Handling Editor: Anne Straube
Received 16 August 2022; Accepted 10 January 2023

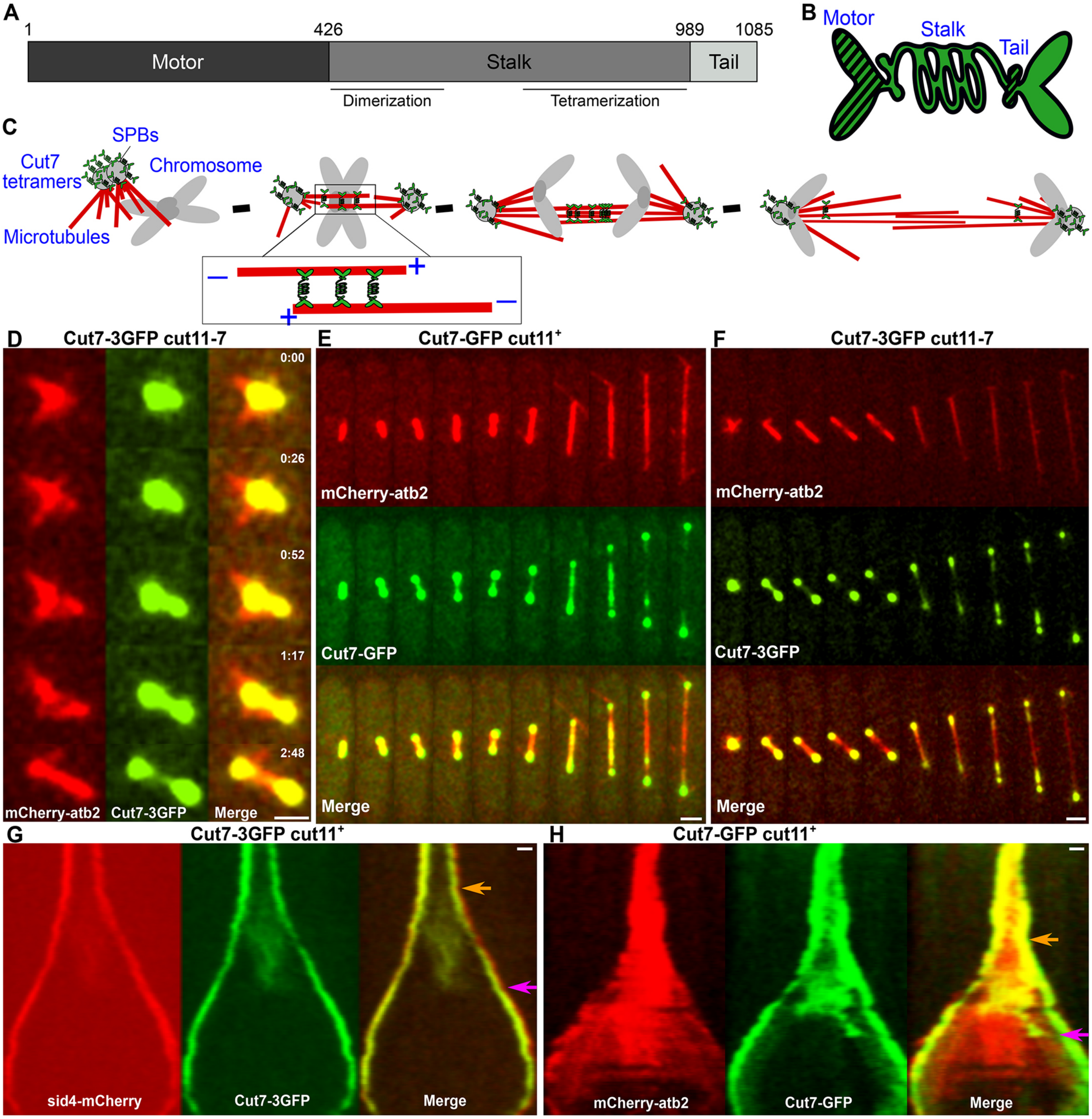

Fig. 1. Overview of Cut7 structure and localization. (A) The major domains of Cut7 delimited by amino acid location. (B) Cartoon of a Cut7 tetramer, showing its 2-fold symmetry. (C) Schematic of localization of Cut7 on a mitotic spindle in *S. pombe*. The magnified box shows Cut7 crosslinking antiparallel MTs. (D) Cut7–3GFP spindle localization in a temperature-sensitive *cut11-7* strain at permissive temperature. As the monopolar spindle becomes bipolar, a subset of Cut7–3GFP (green) moves from the MTs (red) near the left SPB to the MTs near the right SPB. Time is in min:s. Scale bar: 1 µm. (E,F) Example of Cut7–GFP, *cut11+* (E) and Cut7–3GFP, *cut11-7* (F) cells showing Cut7–GFP (green) localization on MTs (red) throughout mitosis. Scale bars: 2 µm. (G) Two-color kymograph of Sid4–mCherry (left), Cut7–3GFP (center), and merge (right). (H) Two-color kymograph of mCherry-atb2 (left), Cut7–GFP (center), and merge (right). Orange arrows mark anaphase B onset; magenta arrows mark the time when visible Cut7–3GFP disappears from the interpolar spindle. Scale bars: 1 µm. The total time of the kymograph in G is 19 min 17 s and for that in H is 25 min 14 s. All images taken at 25°C and are representative of 27 repeats for D,F, 30 repeats for E,H, and 24 repeats for G.

Akera et al., 2015). Truncation or mutation of the tail can decrease or eliminate spindle (Sawin and Mitchison, 1995) or pole (Sharp et al., 1999; Olmsted et al., 2014) localization. Furthermore, tail truncation in the metazoan kinesin-5 Eg5 significantly impairs MT crosslinking and sliding (Weinger et al., 2011; Bodrug et al., 2020), leading to greatly reduced sliding force generation (Bodrug et al., 2020). In budding yeast, deletion of the Cin8 tail is lethal if the second kinesin-5 Kip1 is absent (Hildebrandt et al., 2006), consistent with idea that tail deletion impairs the ability of Cin8 to separate spindle poles. In fission yeast, the pole localization of Cut7 occurs at least in part by direct binding of the tail to γ-tubulin at spindle poles (Olmsted et al., 2014). Recent work has suggested a structural mechanism by which tail–motor interactions could slow ATP hydrolysis (Bodrug et al., 2020). However, the mechanisms by which the C-terminal tail and its phosphorylation affect kinesin-5 motors are incompletely understood.

Previous computational modeling of *S. pombe* spindle assembly suggested that Cut7 bidirectionality might be responsible for its localization at spindle poles for proper spindle assembly (Blackwell et al., 2017; Edelmaier et al., 2020). Simulated bipolar spindles only assembled when kinesin-5 proteins moved bidirectionally. The minus-end-directed movement enhanced the spindle-pole localization of the motors in the model, positioning them to generate force and separate spindle poles (Blackwell et al., 2017; Edelmaier et al., 2020). Experimental work on budding yeast kinesin-5 reached a similar conclusion (Shapira et al., 2017). However, direct experimental testing of these model predictions in fission yeast has been limited because Cut7 bidirectional motility has previously been observed only for the purified motor (Edamatsu, 2014, 2016; Britto et al., 2016). Furthermore, we currently do not understand why (or whether) bidirectional motility and pole localization are beneficial in mitosis, and whether the bidirectional trafficking and motility of kinesin-5 might be altered at different times in mitosis.

Cut7 in the fission yeast *S. pombe* is a useful model for an in-depth study of this bidirectional kinesin on the spindle. This kinesin-5 is well-established as intrinsically bidirectional *in vitro* (Edamatsu, 2014, 2016; Britto et al., 2016). Cut7 is the sole kinesin-5 motor in this organism. It is essential in most genetic backgrounds (Hagan and Yanagida, 1990), but as in other cells, its loss can be rescued by deletion of the two kinesin-14 proteins in cell (Pidoux et al., 1996; Troxell et al., 2001; Rincon et al., 2017; Yukawa et al., 2018, 2020; Lamson et al., 2021). Moreover, Cut7 shares many properties with kinesin-5s more generally, including its basic domain structure and localization (Fig. 1). Study of directional motility on the spindle can take advantage of spindle pole body (SPB) insertion defects in *cut11-ts* cells (West et al., 1998), which lead to monopolar spindles in cells that contain only one active SPB. In mitosis of these cells at restrictive temperature, a spindle MT bundle forms in which all the plus-ends are distal to the single pole, allowing easy assignment of motor movement to polarity (Akera et al., 2015). Fission yeast spindle MTs appear not to undergo poleward flux. This has been demonstrated by photobleaching of anaphase spindles (Mallavarapu et al., 1999; Sagolla et al., 2003), and likely is true throughout mitosis due to the capping of spindle MT minus-ends with γ-tubulin. The lack of poleward flux simplifies the analysis of motor movement on the spindle. Furthermore, *S. pombe* monopolar spindles can enter anaphase with spindle MT elongation occurring at similar speeds to those in bipolar spindles (Masuda et al., 1992; Krüger et al., 2021), facilitating study of changes in kinesin-5 motility before and after anaphase onset. Fission yeast therefore allow study of significant aspects of kinesin-5 function in a cell type that is suitable for detailed analysis.

RESULTS

Cut7 localizes to mitotic spindle MTs and poles in *cut11+* and *cut11-7* cells

To study localization of the kinesin-5 Cut7 and motility on fission-yeast spindles, we constructed strains containing Cut7–GFP and low-level expression of mCherry–tubulin to label spindle MTs (Snaith et al., 2010; Blackwell et al., 2016; Fig. 1D–F, see Materials and Methods). In some cells, we used the SPB component Sid4–mCherry to mark spindle poles (Chang and Gould, 2000). *S. pombe cut7* fused to 1 or 3 GFP molecules at its C-terminal tail can replace the endogenous motor (Fu et al., 2009), and we used both constructs in this study. For simplicity in the text both constructs are referred to as Cut7–GFP. The exact label is noted in the figure panels and legends. The GFP-tagged motor is functional for spindle assembly with no observed growth or mitotic defects, and its localization is similar to that of the endogenous untagged motor (Hagan and Yanagida, 1992). This is consistent with observations of other GFP-tagged kinesin-5 motors (Avunie-Masala et al., 2011; Shapira et al., 2017). Consistent with previous studies (Hagan and Yanagida, 1992; Yukawa et al., 2015), we observed that Cut7–GFP localized to the unseparated spindle poles early in mitosis, and also to the interpolar spindle as mitosis progressed (Fig. 1D–F). We observed similar behavior in *cut11+* cells (Fig. 1E), and in temperature-sensitive *cut11-7* cells (West et al., 1998; Akera et al., 2015) grown at the permissive temperature (Fig. 1F).

Cut7 moves bidirectionally on bipolar spindles with activity that increases in anaphase B

To better assess Cut7 localization and motility during mitosis, we constructed kymographs of Cut7–GFP on bipolar spindles (Figs 1G,H and 2). Two-color kymographs with Sid4–mCherry labeling SPBs (Fig. 1G) or mCherry–atb2 labeling spindle MTs (Fig. 1H) both showed localization of Cut7–GFP near spindle poles throughout mitosis. Therefore, we constructed additional kymographs for analysis using the GFP signal only, where bright spots of Cut7–GFP labeled the ends of the spindle (Fig. 2A–H). As the spindle poles separated, bright clusters of Cut7–GFP appeared on the interpolar spindle. Diagonal streaks of Cut7–GFP signal were visible in the kymographs, which represent directional movement of one or more Cut7 motors (Fig. 2A–H; Fig. S2). These directed movements were both poleward (toward the nearest spindle pole, green arrowheads) and antipoleward (away from the nearest spindle pole, red arrowheads) on bipolar spindles (Fig. 2A–H). To more easily visualize individual or small clusters of Cut7–GFP, we used both photobleaching and photoactivation. After activation of a subset of photoactivatable Cut7–PA-GFP (marked by the blue arrowhead on left SPB in Fig. 2E), we were able to observe poleward and anti-poleward movement of Cut7–GFP. Photobleaching near one spindle pole (marked by blue arrowhead near right SPB in Fig. 2F) allowed additional observation of poleward and anti-poleward movement of Cut7–GFP near that SPB.

We identified the onset of anaphase B as the time when the spindle elongation rate began to increase [Fig. 1G,H, orange arrows, Fig. 2A–D; Krüger et al. (2021)]. Typically the intensity of Cut7–GFP fluorescence near the spindle midzone was highest just after anaphase B onset. In early anaphase B, the kymographs suggested that Cut7 binding and/or movement increased, because a relatively bright, diffuse region of Cut7–GFP intensity appeared (Figs 1G,H and 2A–D, between orange and magenta arrows). Subsequently, most Cut7–GFP intensity disappeared from the interpolar spindle (Figs 1G,H and 2A–D, magenta arrows). After this time, any Cut7–GFP signal visible in the interpolar spindle typically moved toward the nearest spindle pole (Fig. 2G). The midzone of mid-to-late anaphase spindles contained little visible Cut7–GFP, consistent with previous findings showing that the kinesin-6 protein Klp9 contributes more than Cut7 to anaphase B spindle elongation in fission yeast (Yukawa et al., 2018, 2019).

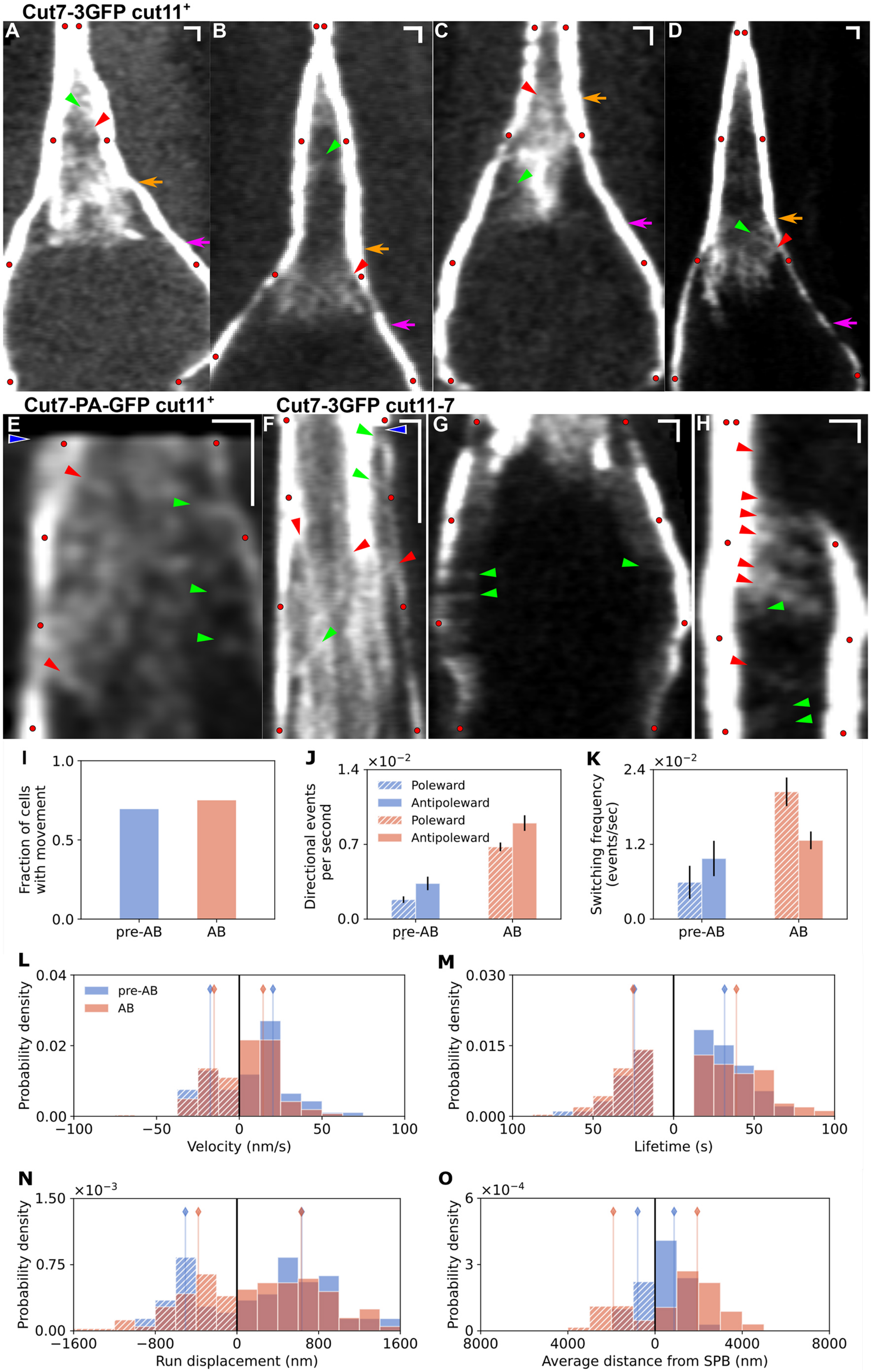

Fig. 2. See next page for legend.

Fig. 2. Localization and motility of Cut7 on bipolar spindles. (A–D) Kymographs of Cut7–3GFP on bipolar spindles from the onset of mitosis through to the end of anaphase. Time reads from top to bottom. Orange arrows mark anaphase B onset; magenta arrows mark the time when visible Cut7–3GFP disappears from the interpolar spindle. Red arrowheads mark anti-poleward movement and green arrowheads mark poleward movement (relative to the nearest SPB). (E) PA-GFP kymograph of Cut7–GFP during anaphase B. The blue arrowhead marks the time of photoactivation near the left SPB. (F) Kymograph with fluorescence photobleaching of Cut7–3GFP during anaphase B. The blue arrowhead marks the photobleaching event near the right spindle pole. Bright tracks (likely clusters of Cut7–3GFP) and dim tracks (likely small clusters or individual motors) are visible. Near the photobleached pole, both poleward and anti-poleward movement is visible. (G) Kymograph in late anaphase B showing poleward movement of Cut7–3GFP that remains on the spindle. (H) Cut7–3GFP localization during spindle pole separation at the onset of mitosis. Cut7–3GFP moves from the left spindle pole and accumulates on the right spindle pole, although the final brightness of the right pole is great enough to suggest that Cut7–3GFP also likely binds directly from the nucleoplasm. SPBs, red circles. Vertical scale bars, 60 s; horizontal scale bars, 1 µm. Images are representative of 39 repeats for A–D, 19 repeats for E, 7 repeats for F, 27 repeats for G, and 39 repeats for H. (I–K) Comparison of Cut7–GFP motility before and after the onset of anaphase B (denoted as AB on the graphs). For quantification, see Tables S1 and S2. (I) Fraction of cells in which visible movement occurred. (J) Frequency of visible directed movement. (K) Switching frequency out of each directed event. Mean±s.e.m. (L–O) Quantification of Cut7–GFP motility events. Values corresponding to poleward-directed movement are on the left side of the axis, anti-poleward directed movement on the right. Vertical bars represent medians of the distributions. For quantification, see Tables S1 and S2. (L) Velocity. (M) Lifetime. (N) Run displacement. (O) Average distance from the spindle pole including all points from each event.

The *S. pombe* interpolar spindle in early mitosis includes some MTs that extend from one pole all the way to the other (Ding et al., 1993; Ward et al., 2015). As a result, poleward and anti-poleward movement cannot be assigned to plus- or minus-end-directed movement. However, in late anaphase, MTs visible in spindle electron micrographs usually overlap only near the spindle midzone (Ding et al., 1993; Ward et al., 2015). Therefore, the poleward Cut7–GFP movement visible near the spindle poles in late anaphase (Fig. 2G) could be minus-end-directed. This suggests that Cut7 can move toward the minus-ends of spindle MTs, consistent with its activity *in vitro* (Edamatsu, 2014, 2016; Britto et al., 2016).

We observed that Cut7–GFP was typically visible near one spindle pole earlier than the other. In *cut11-7* cells, which have SPB insertion defects at the restrictive temperature, we observed that even at permissive temperature, the asymmetry in early Cut7–GFP localization was exaggerated (Fig. 2H). Perhaps this is due to a delay in MT nucleation at the second SPB as observed previously for *cut11-6* cells (Zhang and Oliferenko, 2014). As a result, we observed bright Cut7–GFP signal near one spindle pole and little signal on the other, shortly after the poles separated (Fig. 2H). The kymograph shows that Cut7–GFP traveled primarily toward the dimmer spindle pole. In addition, the signal at the dimmer pole increases rapidly (Fig. 2H). This suggests that some Cut7–GFP pole accumulation likely occurs due to direct binding of the motor to spindle poles, consistent with previous work (Olmsted et al., 2014). In addition, these results suggest that Cut7–GFP moves in both directions between the spindle poles as the bipolar spindle assembles, and that Cut7–GFP signal can increase near a spindle pole due to both movement from the interpolar spindle and direct binding.

To further analyze Cut7 movement, we created custom Matlab software for kymograph analysis (see the Materials and Methods). We hand-traced visible Cut7–GFP tracks and then analyzed events (segments of tracks) that exhibited movement poleward or anti-poleward, or pauses (Figs S1 and S2). Additionally, we divided events into whether they occurred pre and post onset of anaphase B. For each movement event, we analyzed the velocity, lifetime, run displacement and distance from the closest spindle pole. From the entire data set, we identified the total number of cells that showed identifiable directed Cut7–GFP tracks, the frequency at which directional events occurred, and the state exit frequency (the switching frequency, defined as the rate at which a directional event ends by changing direction or pausing; Tables S1 and S2).

Consistent with visual inspection of the kymographs, Cut7 activity significantly increased after the onset of anaphase B (Fig. 2I–K). Before and after anaphase onset, the overall fraction of cells with bipolar spindles imaged that showed visible Cut7–GFP movement was similar, 69% pre-anaphase and 75% in anaphase B (Fig. 2I; Table S1). Despite this similarity, the number of directional events observed per second was larger by a factor of 2–5 after anaphase onset (Fig. 2J). Both pre-anaphase B and in anaphase B, anti-poleward events occurred slightly more frequently than poleward, consistent with the general tendency of Cut7–GFP to accumulate near spindle poles (Fig. 2J). Next, we measured the rate at which directed events ended (switching frequency), either due to pausing or changing direction (Fig. 2K). This rate increased slightly for anti-poleward events, but by a factor of 3 for poleward events in anaphase B, meaning that direction switching and pausing occurred more frequently. Prior to anaphase B, poleward movement had a slightly lower state exit frequency (Fig. 2K), meaning that poleward movement persisted for longer than anti-poleward movement. During anaphase B, the state exit frequency of poleward movement was almost twice that of anti-poleward movement, meaning that anti-poleward movement lasted longer (was more persistent). Therefore, during early anaphase, Cut7 movement events both occurred more frequently and switched direction or paused more frequently.

Analysis of individual directed movement events allowed us to determine motility parameters of poleward and anti-poleward events, both prior to and during anaphase B (Fig. 2L–O; Table S2). Note that to facilitate comparison of poleward and anti-poleward movement, the left half of the graph (negative numbers) show data for poleward movement, whereas the right half of the graph (positive numbers) denote anti-poleward movement (always determined relative to the closest pole at the start of the event). The median speed of Cut7–GFP movement was 15–20 nm s^{-1} for both directions of movement and stages of mitosis (Fig. 2L). Therefore, the change in Cut7 activity in anaphase does not appear to be driven by a change in motor speed. The lifetime of directed events tended to be longer for anti-poleward movement (Fig. 2M). The run displacement was lower for poleward movement and decreased in anaphase B, whereas for anti-poleward events it was higher and stayed the same in anaphase B (Fig. 2N). By averaging all points from all tracks, we measured the average distance of visible tracks from the closest spindle pole and found that this increases by a factor of two in anaphase, reflecting a greater likelihood of Cut7 tracks to be visible farther from the spindle poles in anaphase B (Fig. 2O). We found no significant correlation between Cut7–GFP spot intensity and particle velocity, lifetime, or run length (Fig. S3, pink).

In summary, Cut7–GFP moved in both directions along bipolar spindles, and its direction-switching activity increased significantly in anaphase B. The speed of directed events was typically 15–20 nm s^{-1} and lifetime 10–15 s. Our observation of

Cut7–GFP moving both poleward and antipoleward on bipolar spindles and switching direction was consistent with bidirectional motility on spindle MTs. An alternative way to interpret these movements is to attribute them to Cut7–GFP remaining at plus-ends of growing and shrinking MTs. Therefore we compared the Cut7–GFP event speeds we measured to MT dynamics measurements. Recent work quantified MT dynamics in fission-yeast bipolar spindles in anaphase and found a growth speed of 23 nm s^{-1} and shrinkage speed of 68 nm s^{-1} (Lera-Ramirez et al., 2022). The shrinkage speed is significantly faster than Cut7–GFP poleward movement events that we measured, suggesting that these events likely do not result from motors tracking the plus-ends of depolymerizing MTs. However, the MT growth speed is comparable to the Cut7–GFP movement speed we measured. Therefore, the possibility that Cut7 tracks plus-ends of growing MTs is consistent with our measurements. A potentially complicating factor in assessing directionality of movement is that interpolar spindle MTs are mixed in polarity, making it impossible to assign observed events unambiguously as directed toward plus- or minus-ends of MTs in the diffraction-limited spindle. However, in late anaphase B, results from both electron and light microscopy show that MTs typically end near the midzone: it is rare for an MT from one spindle pole to extend nearly the length of the spindle to end near the opposite spindle pole (Ding et al., 1993; Ward et al., 2015; Lera-Ramirez et al., 2022). Therefore, it is likely (but not guaranteed) that in late anaphase motor movement near the poles is plus-end-directed when anti-poleward and minus-end directed when poleward. To more definitively correlate Cut7 movement with MT polarity, we built on the observation that *S. pombe* monopolar spindles have minus-ends at the SPBs and plus-ends pointing outward. Therefore, we sought to examine Cut7–GFP on monopolar mitotic spindles to determine whether the motor moves both toward plus- and minus-ends of MTs.

Cut7 moves bidirectionally on cut11-7 monopolar spindles

Monopolar mitotic spindles with only one active SPB are observed reproducibly in fission yeast with temperature-sensitive mutations of *cut11* (West et al., 1998). At restrictive temperature, a spindle MT bundle in which all the plus-ends are distal to the single pole forms (Fig. 3), allowing unambiguous assignment of motor movement toward MT plus or minus-ends (Akera et al., 2015). We therefore tracked Cut7–GFP movement on this unipolar MT array to determine whether Cut7–GFP can move toward both the plus- and minus-ends of spindle MTs. For high time resolution of Cut7–GFP movement, we imaged the mCherry–atb2 channel only every 15 timepoints (Fig. S4). We examined these images and chose an MT bundle in the monopolar spindle to construct a kymograph and identify directed Cut7–GFP movement events (Fig. 3; Figs S4 and S5).

In *cut11-7* cells, monopolar spindles initially contained short MTs, similar to those in the bipolar spindles seen in early mitosis (Fig. S4; Fig. 3A,B). Later some of the bundles elongated by almost a factor of two (Fig. S4; Fig. 3C–E). Longer monopolar spindles contained one or more MT bundles that were more stable. The change from short to long monopolar spindles has been shown to occur at the transition into an anaphase-B-like state, based on several cell cycle markers (Krüger et al., 2021), despite the absence of chromosome segregation in these cells. Based on an average of 10 monopolar spindles that showed rapid elongation during our time of observation, we identified 2.4 µm as the length at which this transition typically occurred, allowing us to define a boundary between spindles pre-anaphase and in anaphase B. This allowed us to compare the movement of Cut7–GFP on these two categories of monopolar spindle.

On all monopolar spindles, Cut7–GFP localized primarily near the spindle pole, as observed previously (Fig. S4; Akera et al., 2015). In this case, a kymograph of Cut7–GFP signal appeared as a straight vertical bar with only a few movement events visible along the MT bundle used to construct the kymograph (Fig. S4; Fig. 3A). On the majority of pre-anaphase monopolar spindles, we observed no motion of Cut7–GFP along MT bundles. However, in some cases we observed short, dim events, likely corresponding to single motors or small clusters, characterized by movement a short distance from the SPB and then back (Fig. 3B). In longer anaphase monopolar spindles, brighter clusters were present, which were either paused or moving along the spindle (Fig. 3C–E; Fig. S5). In some cases, we photobleached the signal near the SPB to allow visualization of smaller clusters (Fig. 3C, blue arrow). On these longer monopolar spindles, we often observed Cut7–GFP along spindle MTs more distal to the SPBs (Fig. 3C–E; Fig. S5). In some cases, Cut7–GFP moved in distinct tracks originating from the SPB (Fig. S6). For other events, the Cut7–GFP signal appeared brightly at one point along the spindle, without a clear track leading from the SPB (Fig. 3C–E; Fig. S5). This might occur due to binding of motors directly from the nucleoplasm.

We quantified differences in Cut7–GFP movement on pre-anaphase and anaphase B monopolar spindles, and found that movement of Cut7–GFP away from the SPB occurred more frequently in anaphase B (76% of cells) than were seen on pre-anaphase spindles (31%, Fig. 3F; Table S1). Consistent with this, in anaphase B, the frequency of observable directed events was a factor of 1.5–2 larger for both poleward and anti-poleward movement (Fig. 3G). As a result, anaphase B spindles showed significantly more Cut7–GFP tracks than were seen in cells in pre-anaphase B. The switching frequency out of poleward movement events appeared to increase upon entry to anaphase B (Fig. 3H), consistent with the increase in anti-poleward directed movement.

The median velocity increased slightly on monopolar spindles compared to bipolar spindles (Fig. 3I; Table S2), whereas lifetime and run displacement were somewhat shorter (Fig. 3J,K). These changes were small but might reflect differences in Cut7 behavior during parallel versus antiparallel MT crosslinking, as has been shown for the *S. cerevisiae* kinesin-5 protein Cin8 (Gerson-Gurwitz et al., 2011). The average distance of Cut7–GFP from the SPB was ≈1 µm (Fig. 3L). Together, these data provide evidence that Cut7 motility on the spindle can be toward either the plus or the minus-end of MTs, and there is more motor activity in both directions as cells enter anaphase B.

Cut7–GFP on monopolar spindles showed events moving in both directions, consistent with the idea that the motor moves bidirectionally. However, as mentioned above, such bidirectional events could also occur if the motors can track dynamic MT ends. The median speed of directed Cut7–GFP tracks that we measured on monopolar (and bipolar) spindles was 15–20 nm s^{-1} (Figs 2 and 3; Tables S2 and S3). This is slow compared to previous measurements of fission yeast spindle MT dynamic instability in monopoles, which found an MT growth speed of 45–70 nm s^{-1} and MT shrinking speed of 60–110 nm s^{-1} (Kalinina et al., 2012; Blackwell et al., 2017; Table S3), suggesting that the observed Cut7–GFP movement is unlikely to be due solely to MT plus-end tracking. However, it is possible that MTs with slower dynamics could be present in the spindle. Therefore, we perturbed both MT dynamics and Cut7 motility and examined the effects on Cut7–GFP motility on monopolar and bipolar spindles.

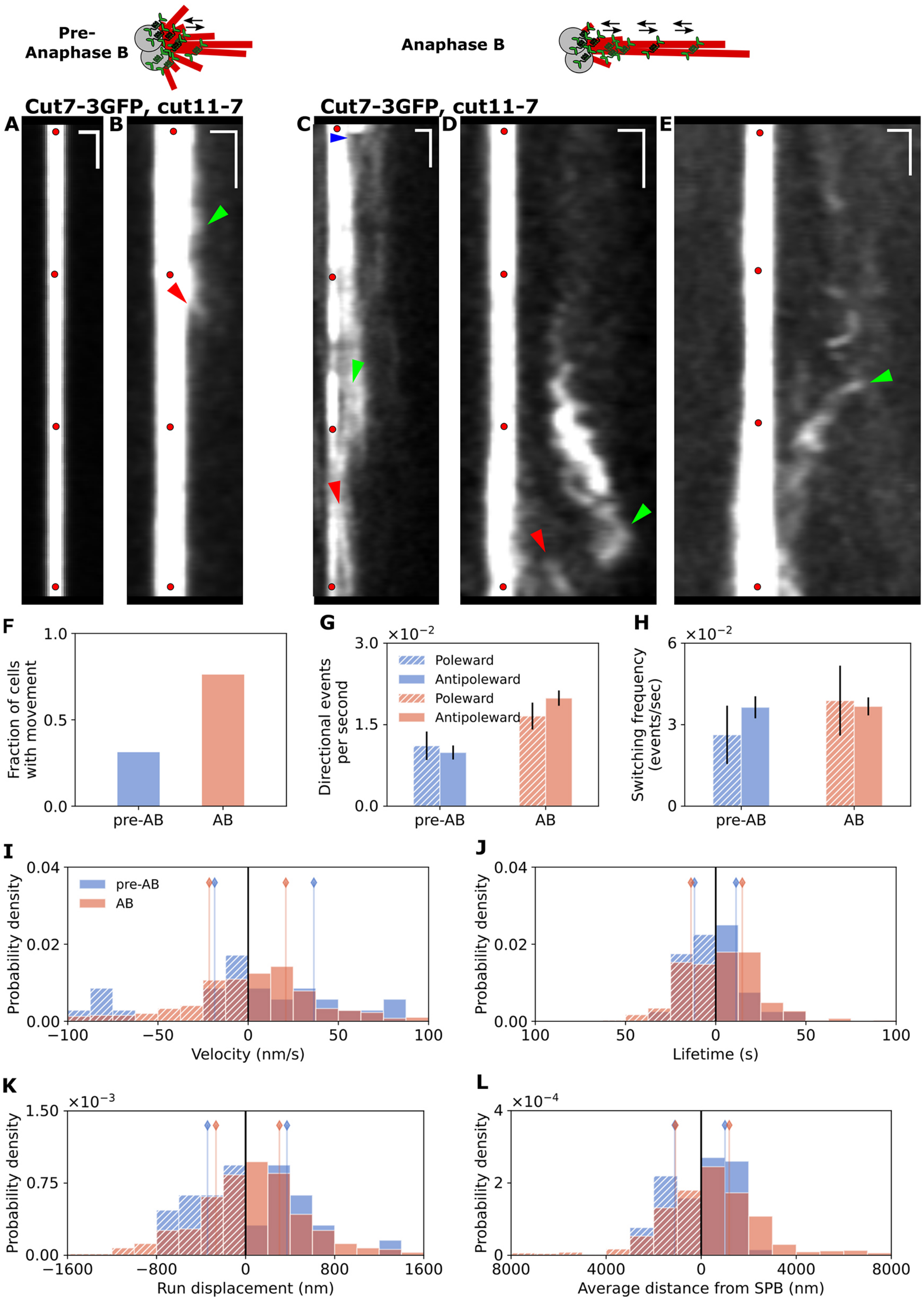

Fig. 3. See next page for legend.

Cut7 moves bidirectionally on *klp5*Δ monopolar spindles, which contain MTs that are more stable

To test whether the observed bidirectional Cut7 movement could be driven by spindle MT dynamics, we imaged Cut7–GFP on *cut11-7* monopolar spindles in cells containing deletions of the kinesin-8 protein Klp5. Because Klp5 contributes to MT depolymerization, *klp5*Δ cells have MTs and spindles that are 2–3 times longer than in wild-type cells (Fig. 4, right versus left cartoon) and are more stable and bundled (West et al., 2001). In addition it has been shown that *klp5* deletion causes no change in the rates of MT growth and

Fig. 3. Localization and motility of Cut7 on monopolar spindles differs in short and long spindles. Schematic of Cut7–GFP movement on monopolar spindles formed in *cut11-7* cells at restrictive temperature. (A–E) Kymographs of Cut7–3GFP on *cut11-7* monopolar spindles. Red arrowheads mark anti-poleward movement and green arrowheads mark poleward movement. (A,B) Pre-anaphase B. (C–E) During anaphase B. (C) Kymograph with photobleaching; the blue arrowhead indicates the time of bleaching the monopolar arm to the right of the spindle pole. SPBs, red circles. Vertical scale bars, 30 s; horizontal scale bars, 1 µm. Images are representative of 74 repeats for A,B,D,E, and 18 repeats for C. (F–L) Comparison of Cut7–GFP motility before and after the onset of anaphase B (denoted AB on the graphs). For quantification, see Tables S1 and S2. (F) Fraction of cells with visible movement. (G) Frequency of visible directed movement. (H) Switching frequency out of each directed event. Mean±s.e.m. (I–L) Quantification of Cut7–GFP motility events. Values corresponding to minus-end directed movement are on the left side of the axis, plus-end directed movement on the right. Vertical bars represent median of the distribution. For quantification, see Tables S1 and S2. (I) Velocity. (J) Lifetime. (K) Run displacement. (L) Average distance from the SPB including all points from each event.

shrinkage; rather it decreases MT dynamicity by reducing the frequency of both rescue and catastrophe (Unsworth et al., 2008). Consistent with previous work, we observed that monopolar spindles in *klp5*Δ *cut11-7* cells were significantly longer than those in *klp5+* (Fig. 4A–E, compare Fig. S7 and Fig. S4). As in *klp5+* cells most Cut7–GFP on *klp5*Δ monopolar spindles remained near the SPB (Fig. S7). If Cut7–GFP bidirectional movement occurred primarily due to MT dynamics, we would expect that Cut7 directional movement would occur less frequently and switch direction less frequently in *klp5*Δ cells compared to *klp5+* cells (Fig. 3).

We found that the fraction of pre-anaphase B cells that showed any spindle-associated Cut7–GFP motion was unaffected by the increased spindle length and was still only 30% (Fig. 4F; Table S1, Fig. S8) despite the longer length of spindle MTs on which events could take place. The fraction of cells with observable movement in *klp5*Δ cells increased during anaphase B to 90%. This fraction was higher in *klp5*Δ cells than in *klp5+* cells (76%). This is the opposite of what would be predicted if MT dynamics drove the observed Cut7–GFP movements.

The number of observable directed Cut7–GFP events per second was similar in the *klp5+* and *klp5*Δ monopolar spindles, but with a slight decrease in the pre-anaphase B-directed movement event rate (Fig. 4G; Table S1). Although the switching rates were comparable in the two strains, the exit rate from anti-poleward movements in anaphase B decreased in *klp5*Δ cells (Fig. 4H; Table S1). This is consistent with the hypothesis that bidirectional movement arises primarily from Cut7–GFP motility. As in *klp5+* cells, motors in pre-anaphase B *klp5*Δ cells switched more frequently to minus-end-directed movement, and they switched more frequently to plus-end-directed movement in anaphase B (Fig. 4H). Overall, Cut7–GFP movement was not dramatically altered by the changing the length and dynamicity of monopolar spindle MTs (Fig. 4I–L; Table S2). The median velocity of directed events decreased slightly compared to that seen in *klp5+*, but the velocity maintained a wide distribution (Fig. 4I). The lifetime increased slightly, again with a wide distribution (Fig. 4J). As a result, the run length (Fig. 4K) was similar to measurements in *klp5+* monopolar spindles. The average distance from the SPB increased in anaphase spindles, likely because the MTs were longer (Fig. 4L). Together, these data are consistent with the idea that that Cut7 moves bidirectionally on spindle MTs. Although movements driven by MT dynamics cannot be completely ruled out, they appear to be a smaller contributor to overall movement than Cut7 intrinsic motility. To further test whether these movements are due to Cut7 motility, we made several perturbations to Cut7 itself.

Bidirectional motility is altered in Cut7 motor and tail mutants

To test whether perturbation of Cut7 can alter its movement on the spindle, we examined alterations to the motor that affect either the motor domain or the C-terminal tail. First, we asked whether Cut7 with no motor activity would change its localization on the spindle. If Cut7 movements are primarily driven by MT dynamics, we would expect to see a similar pattern of localization in motor-active Cut7 and motor-dead Cut7. We therefore created a *cut7* mutant with a motor domain that could not bind ATP (*cut7-motor-dead*), constructed by changing three amino acids at residues 164–166. Previous work showed that this mutation blocks Cut7 movement but not its MT binding (Akera et al., 2015). When *cut7-motor-dead* is the only allele of *cut7* in the cell, it is lethal. Therefore, we expressed it in a strain that also carries the temperature sensitive allele *cut7-446* (Hirano et al., 1986). Of the 25 cells with this genotype we imaged at permissive temperature (25°C), 2 (8%) formed monopolar spindles and 23 (92%) formed bipolar spindles. Unlike Cut7–GFP (Fig. 1) and Cut7-446–GFP (Fig. 5A), Cut7-motor-dead–GFP was not enriched at spindle poles. Instead, it showed faint diffuse fluorescence along the entire length of the spindle (Fig. 5B). Given that Cut7-motor-dead–GFP cannot move along spindle MTs, the diffuse localization appears to result from direct motor binding both at the spindle midzone and near the poles. To further analyze the localization of Cut7-motor-dead–GFP, we made kymographs of the spindle and motor fluorescence (Fig. S9, see Materials and Methods). These showed Cut7-motor-dead-GFP spots that colocalized with spindle MTs, and did not show directed movement along the spindle. Some Cut7-motor-dead–GFP signal was visible near the spindle poles, but did not appear to be enhanced at the poles as occurs in Cut7–GFP (Fig. 2A-D, Fig. S9A,B), or in Cut7-446–GFP (Fig. 5C–F). To compare the localization patterns quantitatively, we selected slices of the kymographs corresponding to specific values of spindle length and averaged GFP intensity across multiple cells with spindles of the same length (see Materials and Methods). Cut7–GFP showed distinct fluorescence peaks at the ends of the spindle, whereas Cut7-motor-dead–GFP shows approximately flat intensity distribution along its length (Fig. S9C–F). Therefore, Cut7-motor-dead–GFP does not appear to have an increased binding preference for spindle poles. This could occur for at least three reasons. First, the motor-dead mutant could be defective in direct binding to γ-tubulin near the SPBs for an unknown reason. Second, perhaps spindle-pole localization requires higher expression of the motor than occurs for *cut7-motor-dead*. Alternatively, the typical spindle localization of Cut7–GFP might depend, at least in part, on its minus-end-directed motility. These results, together with our observations of minus-end-directed Cut7–GFP movement toward spindle poles, suggest that motor movement contributes to Cut7–GFP spindle-pole localization. In addition, this result suggests that while MT dynamics may be a contributor to Cut7–GFP movement, Cut7–GFP accumulation at spindle poles does not occur solely due to MT dynamics.

Next, we sought to determine whether the *cut7-446* temperature-sensitive mutation affects Cut7 motility. This is a single point mutation, I954T, near the start of the tail region (Yukawa et al., 2018). As mentioned above, at permissive temperature these cells formed bipolar spindles with Cut7-446–GFP localization similar to Cut7–GFP (Fig. 5A). Further, kymographs of Cut7-446–GFP appeared similar to those of Cut7–GFP throughout mitosis

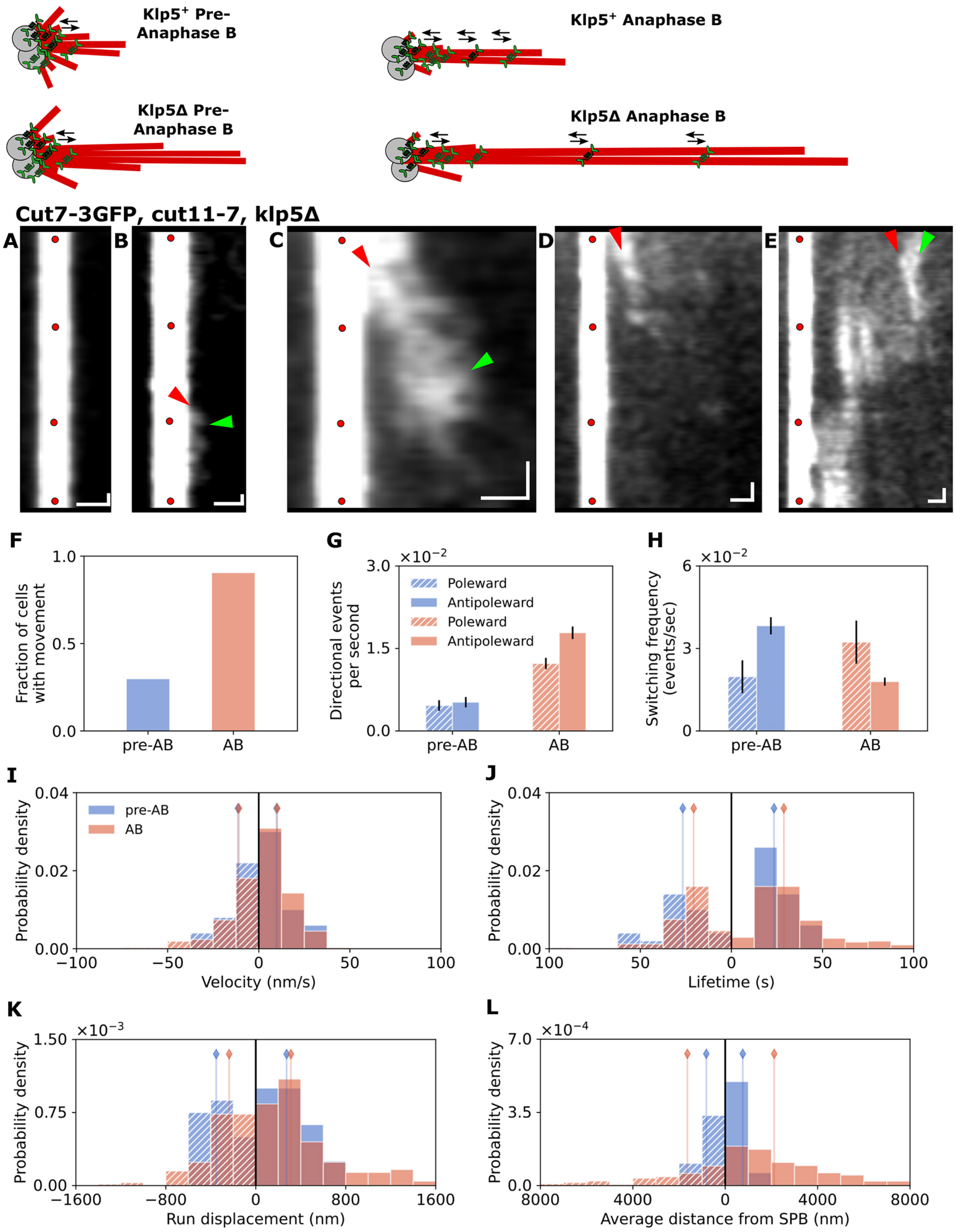

Fig. 4. Longer monopolar spindles make the anaphase B increases in Cut7–GFP motility more evident. Cartoon of Cut7–GFP motor movement on monopolar spindles in *cut11-7* (upper) or in *cut11-7, klp5Δ* cells (lower), before and during anaphase B. (A–E) Kymographs of Cut7–3GFP on *klp5Δ, cut11-7* monopolar spindles. Red arrowheads mark anti-poleward movement and green arrowheads mark poleward movement. (A,B) Pre-anaphase B and (C–E) Anaphase B. SPBs, red circles. Vertical scale bars, 30 s; horizontal scale bars, 1 µm. Images are representative of 78 repeats for A–E. (F–L) Comparison of Cut7–GFP motility on *klp5Δ* monopolar spindles before and after the onset of anaphase B (denoted as AB on the graphs). For quantification, see Tables S1 and S2. (F) Fraction of cells with any movement. (G) Frequency of visible directed movement. (H) Switching frequency out of each directed event. Mean ±s.e.m. (I–L) Quantification of Cut7–GFP motility events. Values corresponding to minus-end directed movement are on the left side of the axis, plus-end directed movement on the right. Vertical bars represent median of the distribution. For quantification, see Tables S1 and S2. (I) Velocity. (J) Lifetime. (K) Run displacement. (L) Average distance from the SPB including all points from each event.

(Fig. 5C–E). We then shifted *cut7-446* cells to restrictive temperature (37°C), which leads to temperature-sensitive lethality by blocking normal SPB separation (Hagan and Yanagida, 1992; Tallada et al., 2009). In 98% of the monopolar spindles that formed (*N*=104), Cut7-446–GFP was visible only near the SPBs, with no directed movement events. This suggests that at restrictive

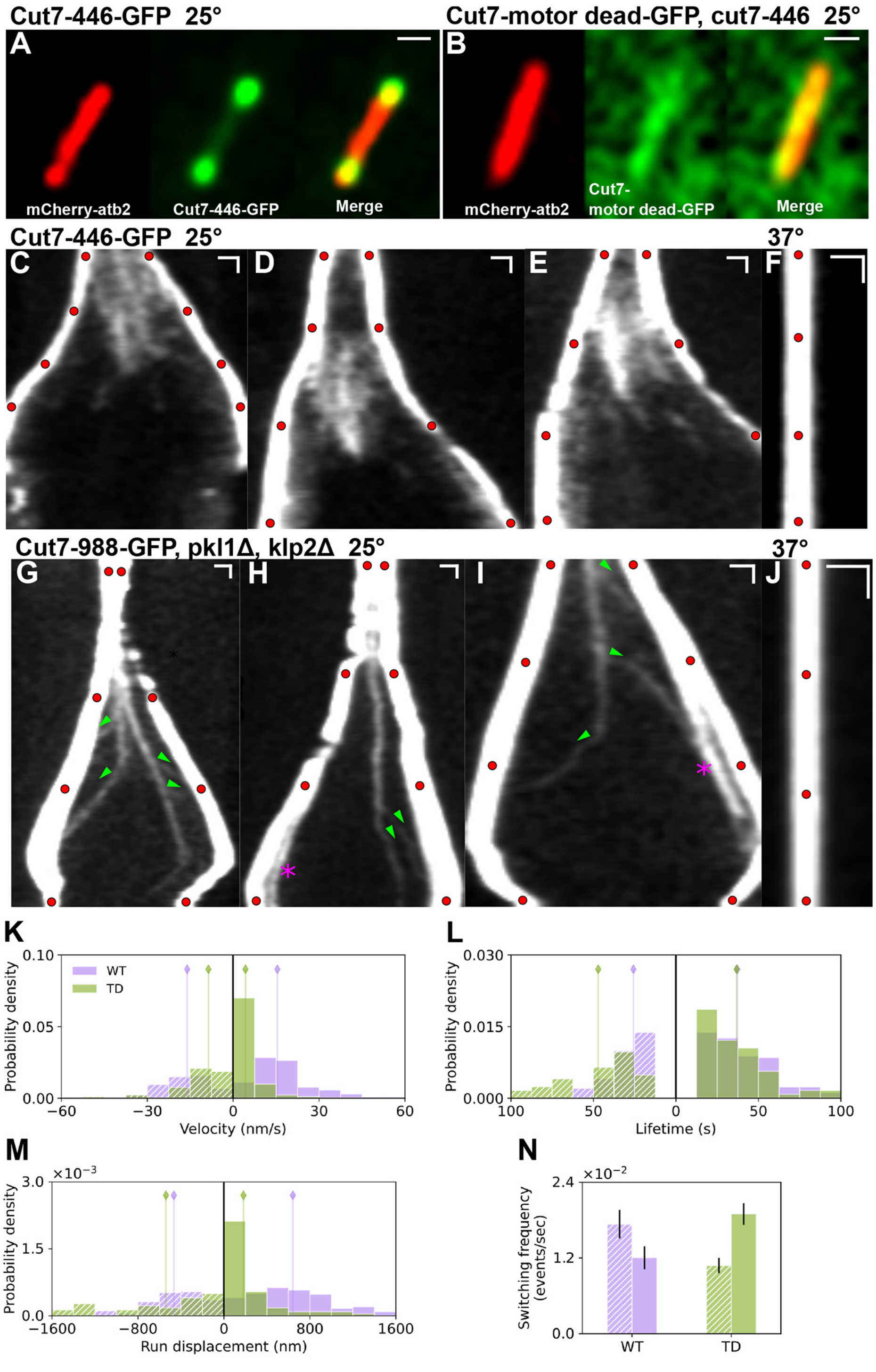

Fig. 5. Mutations in Cut7 alter its motility on bipolar and monopolar spindles. (A,B) Two alleles of Cut7–GFP in *cut7-446* cells at permissive temperature. (A) Dual color image of Cut7-446-GFP (green) on bipolar spindles, demonstrating sparse localization along spindle MTs (red) but normal concentration at the poles (B) Analogous image of Cut7-motor-dead–GFP in *cut7-446* cells, showing some spindle binding but no concentration at the poles. (C–F) Kymographs of Cut7-446—GFP. Bipolar spindles (C–E) at permissive temperature show motility similar to *cut7+* cells whereas monopolar spindles (F) at the restrictive temperature show severely reduced plus-end-directed motility compared to Cut7–GFP. (G–N) Cut7-988–GFP kymographs and data. Removal of the *cut7* tail domain in the absence of *pkl1* and *klp2* leads to reduced motility in bipolar spindles (G–I) and reduced plus-end-directed motility in monopolar spindles (J). SPBs, red circles. Vertical scale bars, 60 s; horizontal scale bars, 1 µm. Images are representative of 28 repeats for A,C–E, 20 repeats for B, 104 repeats for F, 36 repeats for G–I, and 24 repeats for J. (K–N) Comparison of Cut7–GFP (WT) and Cut7-988–GFP (TD) motility. Values corresponding to poleward-directed movement are on the left side of the axis, anti-poleward-directed movement on the right. Vertical bars represent median of the distribution. For quantification, see Table S2. (K) Velocity. (L) Lifetime. (M) Run displacement (N) Switching frequency out of each directed event. Mean±s.e.m.

temperature the motor either cannot move or only retains minus-end-directed motion; we observed almost no plus-end-directed motion (Fig. 5F), in contrast to *cut11-7* monopolar spindles in which Cut7–GFP showed plus-end-directed movements in 36% of spindles (Fig. 3F). This observation is consistent with Cut7 immunofluorescent detection in *cut7-446* cells (Hagan and Yanagida, 1992) and supports that movement of Cut7–GFP is due to its intrinsic motility, and not exclusively to tracking plus-ends of dynamic MTs. In addition, this single amino acid change appeared to abolish or disrupt plus-end movement at the restrictive temperature.

To further perturb Cut7, we truncated the C-terminal tail. The C-terminal tail contains the conserved BimC box containing a Cdk phosphorylation site (Drummond and Hagan, 1998), and point mutations in this region lead to alleles that are temperature sensitive for growth (Rodriguez et al., 2008; Akera et al., 2015). Furthermore, tail truncation in other kinesin-5s can impair MT crosslinking and sliding (Hildebrandt et al., 2006; Bodrug et al., 2020). Therefore we asked whether truncation of the tail at the end of the predicted coiled-coil domain (Fig. S10) affects Cut7 motility. The truncation we constructed removed 96 amino acids from the tail beyond amino acid 988. This mutation appeared to be lethal, as we were unable to produce transformants with *cut7-988* as the sole *cut7* allele in the cell. This is consistent with observations in budding yeast showing that deletion of the kinesin-5 Cin8 tail is lethal in the absence of the kinesin-5 Kip1 (Hildebrandt et al., 2006). To allow observation of motility of Cut7-988–GFP, we examined its phenotype in cells with deletions of *pkl1* and *klp2*, genes that encode two minus-end-directed kinesin-14s. Because Pkl1 and Klp2 are antagonistic to Cut7, deleting them allows study of lethal alleles of *cut7* (Pidoux et al., 1996; Troxell et al., 2001; Rincon et al., 2017; Yukawa et al., 2018, 2020; Lamson et al., 2021). This combination of mutations produced viable cells at 25°C, but monopolar spindles at 37°C.

On bipolar spindles, Cut7-988–GFP localized predominantly to the spindle poles, similarly to Cut7–GFP (Fig. 5G–I). This suggests that the motor has sufficient activity to move to spindle poles or has a binding preference near MT minus-ends, in contrast to Cut7-motor-dead-GFP (Fig. 5B; Fig. S9). However, Cut7-988-GFP appeared present at lower levels on the interpolar spindle than Cut7–GFP in the same strain background (Fig. 5G–I compared to Fig. 2A–D). One possible explanation of the reduced signal intensity in the spindle midzone could be that Cut7-988–GFP is present at lower levels in the cell or is impaired in MT binding. To test this, we compared total intensity of Cut7–GFP and Cut7-988–GFP in line scans along the spindle (Fig. S11). This analysis showed that the integrated intensity is comparable for the two alleles of Cut7 and in fact Cut7-988–GFP showed slightly higher total intensity. Therefore, it appears that the reduced midzone intensity of Cut7-988–GFP likely results from enhanced spindle-pole localization. This suggests that the Cut7 tail might play a role in either plus-end-directed movement or in stabilizing MT binding once the motor has reached the midzone. The Cut7-988–GFP that was observed near the midzone in early mitosis lay in faint clusters with reduced movement (Fig. 5G–I, note that the brightness is increased in these figure panels to make the midzone signal visible; for brightness-matched versions of the kymographs, see Fig. S12). In late anaphase B, however, similar clusters showed processive movement toward spindle poles (Fig. 5G–I, green arrowheads; Fig. S13). The poleward movement typically continued until the signal reached the spindle pole. On monopolar spindles, we observed no plus-end-directed movement (Fig. 5J), consistent with the lethal phenotype of this truncation allele when kinesin-14s are present. Together, these data suggest that Cut7-988–GFP has lost most plus-end-directed motility but retains minus-end-directed motion.

We quantified Cut7-988–GFP movement and compared it to Cut7–GFP movement on bipolar spindles. Because *cut7-988-GFP* cells appeared to show defects in spindle elongation, we could not easily identify the onset of anaphase B from spindle length changes. Therefore, we examined all directed movement events, independently of the stage of mitosis, for both Cut7–GFP and Cut7-988-GFP (Fig. 5K–N; Figs S13, S14A,B, Tables S1 and S2). The speed of Cut7-988–GFP movement was 2–3 times slower than Cut7–GFP, depending on the direction of movement (Fig. 5K). This is in contrast to what is seen for the human kinesin-5 Eg5, which showed faster motility *in vitro* when the tail was truncated (Bodrug et al., 2020). The lifetime of poleward movement events was nearly 2 times longer for Cut7-988–GFP than for Cut7–GFP, whereas the lifetime of anti-poleward movement was comparable (Fig. 5L). As a result, the run displacement of anti-poleward movement was ∼3 times smaller for Cut7-988–GFP than for Cut7–GFP (Fig. 5M). Consistent with this, the switching rate out of anti-poleward movement was higher than the exit rate from poleward movement for Cut7-988–GFP; this is the reverse of the trend for Cut7–GFP (Fig. 5N). As for the full-length protein, we found no significant correlation between Cut7–GFP spot intensity and particle velocity, lifetime or run length (Fig. S3, green).

To test whether the minus-end-directed movement we observed in late anaphase was due to Cut7-988–GFP motor activity or to immobile Cut7 on depolymerizing MTs in the final stages of anaphase, we monitored the time at which the mCherry–tubulin signal in the spindle decreased and the time when Cut7-988–GFP moved poleward. The Cut7 poleward movement typically preceded the MT signal decrease (Fig. S14C,D, white arrowheads). Thus, late anaphase Cut7-988–GFP movement is likely minus-end-directed motor activity. At the same stage of anaphase, we also observed bright fluorescent and relatively immobile clusters of Cut7-988–GFP near the spindle poles (Fig. 5H,I, magenta asterisks).

These results are consistent with the hypothesis that Cut7 bidirectional movement is a result of motor activity, and although MT dynamics might affect its motility it is not the primary cause. The lack of Cut7-988–GFP signal in the spindle midzone could reflect a reduced affinity of the motor for MT overlaps, leading to enhanced binding at the pole. Our quantification of Cut7-988–GFP motility suggests that the C-terminal tail beyond amino acid 988 is a determinant of Cut7 motor activity, with a contribution to plus-end-directed movement.

Human Eg5 that replaces Cut7 shows altered localization and motility on fission yeast spindles

Although several mutations to *cut7* appeared to either abolish its movement or favor MT minus-end-directed motility (Fig. 5), we did not identify *cut7* mutants with a greater propensity for plus-end-directed movement. An alternative protein that can be used to study plus-end-directed movement is the human kinesin-5 Eg5, a plus-end-directed motor that has recently been shown to complement *cut7* as the sole kinesin-5 in *S. pombe* (Hwang et al., 2022). Consistent with prior work, we found that cells containing Cut7–GFP or Eg5–GFP expressed at low levels in the *cut7* deletion background were viable (Fig. 6; Fig. S15). Whereas Cut7–GFP localized brightly to the spindle poles and more dimly along spindle MTs (Fig. 6A), Eg5–GFP was visible along the spindle with little to no enhancement at the poles (Fig. 6B). To further examine the dynamics of motor localization over time, we compared kymographs of Cut7–GFP and Eg5–GFP on bipolar spindles. The pole localization was noticeable for Cut7–GFP (Fig. 6C), whereas Eg5–GFP is visible at the spindle poles only rarely and transiently (Fig. 6D). We also observed that in Eg5–GFP cells, initial spindle pole separation often occurred more quickly and was followed in ∼20% of cells by spindle shortening events (Fig. 6D). These results suggest that when a purely plus-end-directed kinesin-5 motor is present on the fission yeast spindle, it may be over-active and drive premature spindle elongation followed by shortening.

This relatively uniform Eg5–GFP spindle localization is consistent with our other results suggesting that the bidirectional motility of Cut7 contributes to its pole localization; plus-end-directed Eg5 would therefore not be predicted to accumulate at the spindle poles. In addition, Eg5–GFP fluorescence visible both at the spindle midzone and near spindle poles is consistent with direct motor binding along the length of the spindle. Eg5–GFP might therefore show different localization from Cut7–GFP in part because Cut7 binds directly to γ-tubulin at spindle poles (Olmsted et al., 2014).

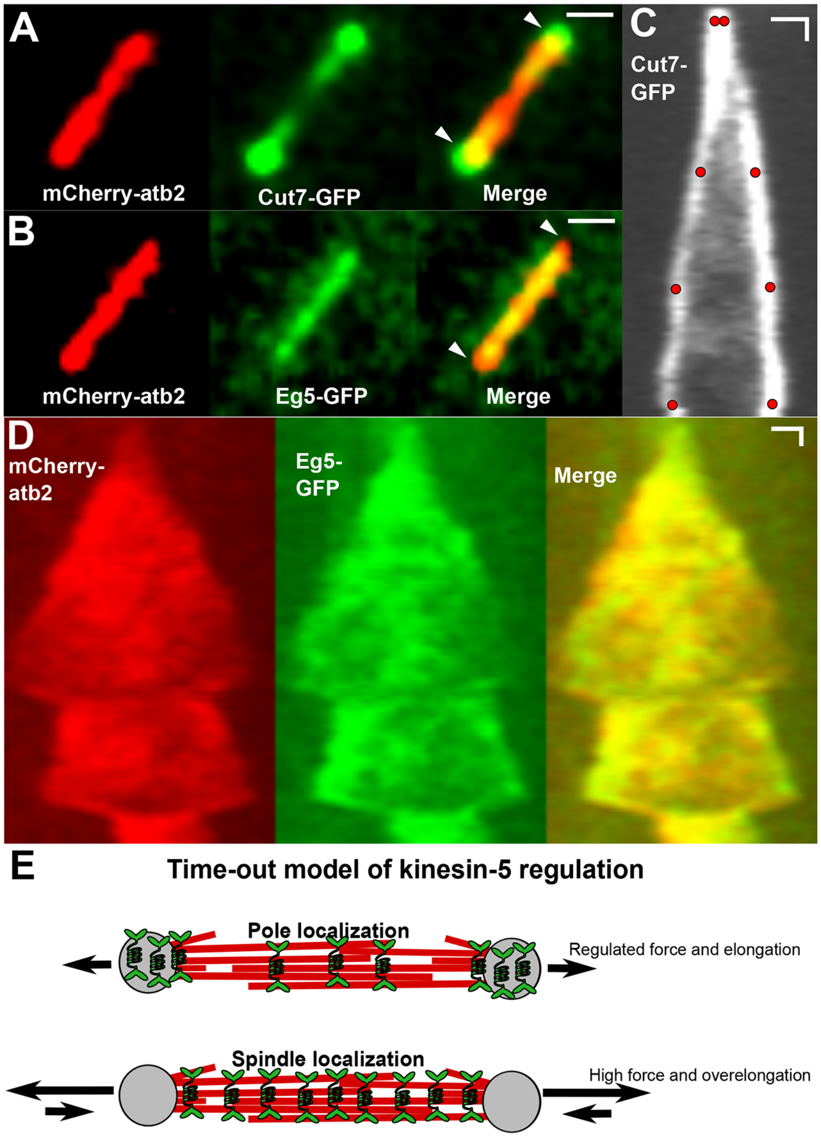

Fig. 6. Eg5–GFP shows altered localization on bipolar spindles. (A,B) Dual color images of bipolar spindles. (A) Cut7–GFP (green) showing typical enrichment at the SPBs (arrowheads) and binding along the MTs (red). (B) SPB enrichment in Eg5–GFP (green) is no longer present (arrowheads) and Eg5–GFP binds uniformly along the spindle. (C,D) Kymographs of bipolar spindles. (C) Cut7–GFP shows consistent SPB enrichment and movement along the interpolar spindle. (D) Eg5–GFP shows reduced SPB enrichment and more uniform localization along spindle MTs. Spindle shortening events also occur in the Eg5-GFP. SPBs, red circles. Vertical scale bars, 60 s; horizontal scale bars, 1 µm. Images are representative of 18 repeats for A,C, and 25 repeats for B,D. (E) Schematic model illustrating the hypothesis that spindle-pole localization may sequester kinesin-5 motors to regulate force generation.

DISCUSSION

Cut7–GFP moves bidirectionally on spindle MTs with regulated motility

Our results show that Cut7 can move in cells toward both plus- and minus-ends of mitotic MTs, similar to its bidirectional motility *in vitro* (Edamatsu, 2014, 2016; Britto et al., 2016). After verifying that Cut7–GFP localized on the spindle, as observed in previous work (Fig. 1; Hagan and Yanagida, 1992; Drummond and Hagan, 1998; Yukawa et al., 2015), we examined the directional movement of Cut7–GFP on both bipolar and monopolar spindles. The Cut7–GFP fluorescent signal moved in both directions along bipolar spindles (Fig. 2), which is consistent with bidirectional motility but does not definitively demonstrate it because the spindle contains extensive overlapping antiparallel MTs. The bidirectional movement also occurred on monopolar spindles that contained MTs of only one orientation (Figs 3 and 4). We note that Cut7–GFP movement on bipolar and monopolar spindles was similar and occurred during a comparable time in mitosis in all cells. The similar motility observed therefore suggests that motor direction is defined by features of the motors themselves, rather than being strongly influenced by MT polarity and parallel versus antiparallel crosslinking. Consistent with this view, we observed that individual fluorescent spots can change their direction of motion (Fig. 3D–G; Figs S5 and S8).

The speed of directed events that we measured was ~15–30 nm s^{-1} for both directions of movement (Figs 2L and 3I; Table S2). In previous experiments with purified Cut7, surface-bound motors were found to drive MT motion in gliding assays at similar speeds, of ~10–30 nm s^{-1} (Edamatsu, 2014; Britto et al., 2016), although the speed was higher (~200 nm s^{-1}) for minus-end-directed movement at low concentration (Britto et al., 2016). The motion of Cut7 on single MTs occurred at 150–200 nm s^{-1} (Edamatsu, 2016). Thus our velocity measurements are consistent with the slower range of speed measured *in vitro* and the speed of Eg5 *in vitro* (Bodrug et al., 2020).

Our findings suggest that although Cut7 movement has a stochastic component, it is regulated and changes as mitosis progresses. In particular, we found that the activity of Cut7–GFP increased at anaphase B onset on both bipolar and monopolar spindles. We observed a larger percentage of cells that showed Cut7–GFP movement, a greater frequency of directed events, and an increased rate of switching in anaphase B (Figs 2–4; Table S1). We speculate that phosphoregulation of Cut7 could play a role in this change in activity, as has been previously demonstrated for the budding yeast kinesin-5 Cin8 (Avunie-Masala et al., 2011; Shapira and Gheber, 2016). The *cut7* C-terminal tail contains several conserved phosphorylation sites, including a Cdk consensus site in the BimC box (Heck et al., 1993; Sawin and Mitchison, 1995; Blangy et al., 1995; Drummond and Hagan, 1998; Cahu et al., 2008; Rapley et al., 2008; Akera et al., 2015). In addition, multiple sites in the *cut7* tail have been shown to be phosphorylated in cells using mass spectrometry analysis (Wilson-Grady et al., 2008; Koch et al., 2011; Kettenbach et al., 2015). This makes tail phosphorylation of interest for future study.

These observations of increased Cut7–GFP activity and fluorescence signal in the spindle midzone is consistent with Cut7 having a contribution to anaphase spindle elongation (Yukawa et al., 2019; Fig. 2). The fact that most Cut7–GFP signal disappears from the spindle midzone not long after anaphase B starts is also consistent with previous work showing that the kinesin-6 Klp9 is the primary motor driving spindle elongation in *S. pombe* (Fu et al., 2009). By late anaphase, the Cut7–GFP still visible on the spindle appears to be primarily minus-end-directed, and thus likely does not contribute significantly to spindle elongation (Fig. 2G). Therefore, it is likely that any contribution of Cut7 to spindle elongation by antiparallel MT sliding occurs early in anaphase.

Motor and tail domains both contribute to Cut7 bidirectional motility and pole localization

We find that both the motor and C-terminal tail domains of Cut7 contribute to its bidirectional movement and localization. The tail mutations we examined appeared to limit the motility of Cut7 toward MT plus-ends, which suggests that the ability of Cut7 to move toward MT plus-ends is more fragile that its minus-end-directed motion. Both a point mutation in the tail region (*cut7-446*) and tail truncation (*cut7-988*) favor the localization of the motor to the pole and appear to reduce its plus-end-directed motility (Fig. 5F,J). The results also point to a role of the C-terminal tail domain as a site for motor regulation. Some properties or modification of the tail might be important for inducing plus-end-directed motion of Cut7.

Although wild-type *S. cerevisiae* Cin8 localizes to the minus-ends at the SPB of pre-assembled (monopolar) spindles, a mutant lacking the C-terminal tail (but still containing a nuclear localization signal) localizes to the plus-ends of monopolar spindles (Shapira et al., 2017). On bipolar spindles, this mutant localizes similarly to wild-type Cin8, at the spindle poles and the interpolar spindle (Düselder et al., 2015). Therefore, the tail truncation of Cin8 appears to favor its plus-end-directed motility. In contrast, here we show that the Cut7-988–GFP tail deletion mutant, compared to the full-length protein, shows an increased bias toward the poles of both bipolar and monopolar spindles.

Truncation of the human kinesin-5 Eg5 tail causes it to move more quickly and cluster less *in vitro*, possibly because tail–motor interactions alter the motor conformation to slow ATP hydrolysis (Bodrug et al., 2020). In contrast, we find in cells that the tail-truncated Cut7-988–GFP moves more slowly; however, we also see decreased clustering. Despite these differences, both motors appear to be impaired in sliding MTs, given that *cut7-988* is lethal when it is the only *cut7* allele present in the *pkl1*$^+$ *klp2*$^+$ background. For Eg5, decreased MT sliding force generation has been directly measured *in vitro* (Bodrug et al., 2020), and our results indirectly suggest that Cut7-988 has defects in force generation because it is lethal unless the opposing kinesin-14s are also deleted.

The bidirectional movement of Cut7 that we observed could in principle be driven by tip-associated Cut7 on dynamic spindle MTs. To test this idea, we examined how Cut7–GFP localization and motility changed in cells when MT dynamics or Cut7 motility were perturbed. Deletion of the kinesin-8 Klp5 induces elongation of cellular MTs and decreases their dynamicity (Unsworth et al., 2008). We found that Cut7–GFP motility showed only subtle changes on monopolar spindles in *klp5*Δ cells (Fig. 4), supporting that idea that MT dynamics are not the primary driver of the observed Cut7–GFP movement. In contrast, perturbations to Cut7 itself did lead to changes in its localization and motility (Fig. 5). Our observation that Cut7 accumulates poorly at SPBs when its ATPase activity is eliminated (Fig. 5B) provides evidence that Cut7 spindle pole accumulation is at least in part motor driven. Consistent with this idea, plus-end-directed human Eg5 can replace Cut7 in *S. pombe* (Hwang et al., 2022; Fig. S15), but does not strongly localize to spindle poles (Fig. 6). We conclude that Cut7 motor activity contributes to the directed movement we have described.

Function of fission yeast versus budding-yeast kinesin-5s

The budding yeast *S. cerevisiae* contains two kinesin-5s, Kip1 and Cin8. Of these, Cin8 appears to be more similar to Cut7 (51.2% BLAST sequence identity versus 35.4% sequence identity with Kip1). Both budding yeast motors are strongly localized to the spindle poles and more weakly at or near the spindle midzone, but neither of them accumulates there until some time into anaphase (Gerson-Gurwitz et al., 2011; Fridman et al., 2013). This pattern of localization is somewhat similar to that of of Cut7 in *S. pombe*. However, Cut7 does not concentrate at the midzone in late anaphase, as Cin8 does, probably reflecting the fact that the kinesin-6 Klp9 is important for late anaphase B spindle elongation in fission yeast, whereas the kinesin-5s play this role in budding yeast. Both Cin8 and Cut7 have been shown to be bidirectional *in vitro* (Roostalu et al., 2011; Gerson-Gurwitz et al., 2011; Edamatsu, 2014, 2016; Britto et al., 2016), and Cin8 also moves bidirectionality on spindle MTs *in vivo* (Gerson-Gurwitz et al., 2011; Fridman et al., 2013). Our work thus confirms that Cut7 moves bidirectionally on the spindle *in vivo* as well. Both motors are important for separation of SPBs to establish a bipolar spindle (Hoyt et al., 1992; Roof et al., 1992; Hagan and Yanagida, 1990, 1992; Tallada et al., 2009), suggesting that both exert plus-end-directed forces early in mitosis. In contrast to Cut7, Cin8 appears to persist in this role throughout mitosis, whereas Cut7 passes that role on to a different motor.

In *S. cerevisiae*, distinct processive Cin8 tracks appear common (Gerson-Gurwitz et al., 2011). In *S. pombe*, clear tracks can be identified, but appear to be less common (Fig. 2). Instead, a region of dim Cut7–GFP fluorescence is visible along the spindle. We observed distinct tracks occasionally in cells with Cut7–GFP and frequently in cells with the tail truncated Cut7-988–GFP (Fig. 5G–I). Therefore, the region of dim Cut7–GFP fluorescence on bipolar spindles likely reflects combined movement of many motors.

The minus-end-directed motility of Cin8 depends on phosphorylation in the motor domain on Cdk1 sites not conserved in *cut7* (Shapira and Gheber, 2016). By contrast, we find that the Cut7 perturbations we examined decreased or abolished plus-end-directed movement. Our results therefore suggest that Cut7 is more intrinsically minus-end-directed and acquires plus-end directionality by some mechanism that has not yet been clearly identified. This may be due to motor crowding (Britto et al., 2016), phosphorylation analogous to the regulation of Cin8, or some other mechanism.

Function of Cut7 bidirectional motility and pole localization

It is well established that kinesin-5s are able to crosslink and slide antiparallel MTs to separate spindle poles, a function which depends on plus-end-directed motility of kinesin-5 tetramers. Our work further supports the importance of kinesin-5 plus-end-directed motility, because the temperature-sensitive *cut7-446* and *cut7-988* alleles that show either no motility or reduced plus-end-directed events on monopolar spindles at 37°C are unable to create a bipolar spindle (Fig. 5F,J). Consistent with this, *cut7-motor-dead*, which does not move on bipolar spindles (Fig. S9), is lethal when it is the sole *cut7* allele in the cell (Akera et al., 2015). Given the importance of plus-end-directed motility, the importance of bidirectional motility and trafficking, and pole localization has been less clear.

In previous work, we used a computational model of *S. pombe* spindle assembly to propose that localization of the kinesin-5 Cut7 near the spindle poles might be required for proper spindle pole separation (Blackwell et al., 2017; Edelmaier et al., 2020). This was based on model simulations in which a processive, purely plus-end-directed kinesin-5 localized far from the SPBs in monopolar spindles and failed to separate spindle poles. Experimental work on budding yeast Cin8 reached a similar conclusion (Shapira et al., 2017). However, the experimental results we present here appear to rule out that hypothesis. Importantly, human Eg5 can replace *cut7* and assemble a bipolar spindle (Hwang et al., 2022) despite being a plus-end-directed kinesin-5 and not significantly localizing to *S. pombe* spindle poles (Fig. 6). Therefore, minus-end-directed motility is not required for bipolar spindle assembly in fission yeast. How to reconcile this with the computational modeling results is an interesting question for future work. We speculate that perhaps Eg5 has higher turnover that allows it to unbind and avoid becoming localized primarily at the plus-ends of spindle MTs in early mitosis.

We observed that replacement of Cut7 with low-level expression of Eg5 in *S. pombe* can lead to faster initial separation of spindle poles, a longer spindle and transient spindle shortening (Fig. 6D). Additionally, recent work found that high-level expression of either human Eg5 or Cut7 in *S. pombe* was lethal with over-elongated spindles (Hwang et al., 2022). Together, these results suggest that a highly expressed or purely plus-end-directed kinesin-5 that localizes along spindle MTs might produce excessive sliding force that over-elongates the spindle. Therefore, we propose a new hypothesis that spindle-pole localization of kinesin-5 might sequester the motor in a ‘time out’ at a location where its sliding activity is low (Fig. 6E). In this view, the spindle pole localization might decrease motor activity. Testing this model will be the subject of future work.

MATERIALS AND METHODS

Strain construction by crossing

Cells were cultured using standard techniques (Moreno et al., 1991). Existing strains (Table S4) were crossed, and the desired genotypes isolated using random spore analysis. The *cut11-7* and *cut7-446* mutations were identified by replica plating colonies from the spore analysis onto YE5S plus phloxin B (BD Biosciences BD for YE media, Sigma for 5S supplements and phloxin B) agar plates. After 2–3 day at 37°C, dark-pink colonies were identified as positive for the mutations. All other genes were identified using Edinburgh minimal medium (EMM; MP Biomedicals) plates without the relevant supplement for auxotrophic mutants or YE5S plates with the relevant antibiotic. The fluorescent label for MTs was obtained by expressing an mCherry–α-tubulin-chimera at a low level (~10% of wild-type α-tubulin), as used previously (Yamagishi et al., 2012; Gergely et al., 2016; Blackwell et al., 2017). This low-level labeling reduces possible tag-related perturbations to MT dynamics. Cells with kinesin-5 mutation or deletion are susceptible to chromosome missegregation and other mitotic abnormalities. To avoid problems resulting from these abnormalities, cells for each experiment were stored at 4°C and reisolated from frozen stocks every 2–4 weeks.

Plasmid and strain construction by molecular biology

Oligonucleotide primers were purchased from Integrated DNA Technologies (Coralville, IA). Restriction enzymes and Phusion HF DNA polymerase were purchased from New England Biolabs (Ipswich, MA). DNA was prepared using Qiaprep Spin Miniprep Kit and PCR products were purified using Qiaquick PCR Purification Kit, both from Qiagen (Germantown, MD). *S. pombe* genomic DNA was prepared using YeaStar Genomic DNA Kit from Zymo Research (Irvine, CA). DNA sequencing was performed by Quintarabio (Hayward, CA). The DNA concentration was determined using a Thermo Scientific Nanodrop 2000. Strains were verified by PCR and sequence analysis of genomic DNA. At least two different transformant strains were analyzed in experiments.

Strain construction for Cut7–photoactivatable-GFP

PA-sfGFP (Addgene 54579) was amplified by PCR using oligonucleotide primers Pac1-paGFP-F (5′-GGGTTAATTAACGTGAGCAAGGGCGAGGAG-3′) and Asc1-paGFP-R (5′-AGTGGCGCGCCCTACTTGTACAGCTCGTCCATGCC-3′) and the product was cloned into pFA6a-GFP(S65T)-kanmx6 (Addgene 39292) digested with Pac1/Asc1. The resulting plasmid was amplified by PCR using oligonucleotide primers Cut7-Cterm-pFA6a-GFP/paGFP-F (5′-AATTCATCAAGAACTAGTCTTTTGCGGAGTAGCAGAAGTGCCTATTCCAAAATGAAACGACGGATCCCCGGGTTAATTAA-3′) and Cut7-Cterm-pFA6a-GFP/paGFP-R (5′-GATGTAATACATTTCTATTGTATTTTCGTCCATTAAGTATAAATTAATAAAATCGTGTCAGAATTCGAGCTCGTTTAAAC-3′) and the product was used to transform *S. pombe* using a lithium acetate method (Okazaki et al., 1990).

Strain construction for Cut7-446–GFP and Cut7-988–GFP

For *cut7-446-GFP*, strain MB921 was transformed with PCR product obtained using plasmid pFA6a-GFP(S65T)-kanmx6 (Addgene 39292) and oligonucleotide primers Cut7-Cterm-pFA6a-GFP/paGFP-F and Cut7-Cterm-pFA6a-GFP/paGFP-R as above. For *Cut7-988-GFP*, strain MB1147 was transformed with PCR product obtained using plasmid pFA6a-GFP(S65T)-kanmx6 (Addgene 39292) and oligonucleotide primer Cut7-988-Cterm-pFA6a-GFP-F (5′-TTAAAGGGAACGACATCACTTGCTAATCATACTAATGAATTACTTGGTTTAGGAGATGAACGGATCCCCGGGTTAATTAA-3′) and Cut7-Cterm-pFA6a-GFP/paGFP-R as above. The choice to truncate at amino acid 988 was based on coiled-coil prediction (Lupas et al., 1991; Fig. S10). All of these *cut7* alleles contain the identical single GFP molecule separated from the *cut7* open reading frame by a six amino acid linker (RIPGLI).

Strains expressed from heterologous promoter

The genes for *cut7*, *cut7-motor-dead* and Eg5 were cloned using PCR into plasmid 462 (Addgene 89065) containing a Z3EV promoter (Ohira et al., 2017) modified to contain Asc1/Srf1 sites just upstream of the GFP gene. The motor dead mutation (G164A-K165A-T166A) was cloned by PCR from strain PB951 (MB947, Akera et al., 2015) into the 462-cut7 plasmid. These alleles all contain the identical single GFP molecule (as for the *cut7* alleles discussed above), but for these *cut7* alleles the linker is three amino acids (SRA). For the Eg5 allele expressed under the heterologous promoter, there was no linker before the GFP. These plasmids were cut at Aatll and integrated at the *his7* gene in Strain FY31411 (yFS949, MB1138). The strain was crossed to produce strain MB1164. Estradiol was not used in our experiments; rather *cut7* or Eg5 were expressed at a constitutive lower level.

Live-cell imaging

All microscopy images and related datasets were obtained from confocal microscopy using live-cell preparation. Cells were grown at 25°C on YE5S plates for 48 h and restreaked every 12 h. A small volume of exponentially growing cells was removed from the Petri dish and placed in 10 µl of EMM. EMM was filtered with a 0.2 µM cellulose acetate filter (VWR

International) to reduce background fluorescence. Cells in EMM were placed on 22×60-mm coverslips pretreated with 8 µl of lectins from *Bandeiraea simplicifolia* (Sigma-Aldrich). These coverslips were pre-equilibrated to the appropriate temperature of either 25 or 37°C. Bipolar spindles were imaged at 25°C and monopolar spindles were imaged at 37°C. To obtain sufficient monopolar spindles, *cut11-7* cells were placed at 37°C for 2–4 h and then imaged at the restrictive temperature. Cells were transferred from a 37°C incubator to the pre-warmed microscope in less than 30 s to prevent monopolar spindles cooling down and possibly becoming bipolar. Temperature was maintained with ±0.1°C precision using a CherryTemp temperature controller (Cherry Biotech, Rennes, France). Spinning-disk confocal microscopy was performed on a Nikon Eclipse Ti microscope described previously (Gergely et al., 2016; Blackwell et al., 2017; Edelmaier et al., 2020). Time-lapse image stacks were obtained using the EM gain laser settings on the Nikon illumination system and the number of *Z*-planes described previously (Edelmaier et al., 2020).

PA-GFP and fluorescence photobleaching experiments

Photoactivation experiments used a 405 nm, 50 mW coherent Obis laser (Santa Clara, CA). Before photoactivation, 4 image stacks with illumination from the 561 nm and 488 nm lasers were obtained to record the location of the MTs and confirm that no GFP signal existed prior to activation. Photoactivation was then performed on either a monopolar MT bundle or near the spindle pole with the laser at 10% power and an exposure time between 15 and 1000 ms. After photoactivation, time-lapse image stacks were obtained continuously using the 488 nm illumination laser. For fluorescence photobleaching experiments, the same 405 nm laser was used. Before photobleaching, four image stacks with illumination from the 488 nm laser were obtained to record the location of the spindle poles and Cut7–GFP. Photobleaching was then performed on the area of interest with the laser at 50–100% power and an exposure time of 100 ms. After photobleaching, signal was measured with time-lapse image stacks obtained continuously using the 488 nm illumination laser.

Determination of spindle length for pre-anaphase and anaphase B

Ten monopolar spindles each for *klp5+* and *klp5*Δ cells that underwent rapid elongation after a period of a constant, stable length were identified. The average length at this transition for *klp5+* spindles was 2.40 µm, and for *klp5*Δ spindles was 5.16 µm.

Dataset organization and kymograph creation

For all bipolar tracked data in this study, strains with Cut7–GFP or Cut7–3GFP, and *cut11+* or *cut11-7* were pooled to create the kymographs and associated datasets displayed in Figs 2–5. In addition, PA-GFP and fluorescence photobleaching experiments were pooled with all non-PA-GFP and unbleached experiments to create datasets for Figs 2,3. The kymographs used for the quantification in Fig. 2 were compiled from strains MB951, MB1030, MB1032, MB1062, MB1064, MB1077 and MB1085 (Table S4). The kymographs quantified for Fig. 3 were compiled from strains MB951 and MB1088 (Table S4). The monopolar spindles analyzed in Fig. 4 were compiled from strain MB1134. The bipolar spindles analyzed in Fig. 5 were compiled from strains MB1131 and MB1155 and compared with the pooled data from Fig. 2.

All confocal images were transferred as Nikon nd2 files into the Fiji version of ImageJ (National Institutes of Health, Bethesda, MD) and displayed as pixel-interpolated, maximum-intensity projections. The Fiji plugin StackReg was utilized to align the data using the Transformation-Rigid Body option. The ImageJ segmented line tool was used to draw a straight line through the aligned spindle data. Finally, the ImageJ Reslice function with an output spacing of 1 µm was used to create the kymographs shown.

Kymograph preparation and analysis for Cut7-motor-dead

To prepare the Cut7-motor-dead-GFP kymographs (Fig. S9), we identified the spindle axis direction and the centrosome location using the Toolkit for Automated Microtubule Tracking (TAMiT, https://github.com/Betterton-Lab/TAMiT.git). Based on spindle length and position fit by TAMiT, we defined and aligned a constant-length axis along the spindle using the red channel in every frame. We then used Matlab to interpolate the pixel intensity along the defined axis to make kymographs for both channels (MT and Cut7-motor-dead-GFP; Fig. S9A,B). The brightness and intensity of each channel of the kymograph are adjusted independently in FIJI before merging.

To measure the GFP intensity distribution along the spindle axis for both Cut7–GFP and Cut7-motor-dead–GFP (Fig. S9C–F), we identified slices from kymographs corresponding to spindle lengths of 1, 2, 3 and 4 µm, ±0.1 µm around this length. The Cut7–GFP kymograph line-scans were retrieved from 29 Cut7–GFP kymographs, and from seven Cut7-motor-dead–GFP kymographs. All individual line scans were aligned based on one of the spindle-pole positions (chosen to be the pole with brighter intensity for Cut7–GFP imaging and chosen at random for Cut7-motor-dead–GFP imaging). We then averaged all line scans for the relevant spindle length and plotted the average *cut7* intensity distribution along the spindle axis.

Total intensity analysis for Cut7–GFP and Cut7-988–GFP

To quantify the total GFP intensity along the spindle axis for both Cut7–GFP and Cut7-988–GFP (Fig. S11), we identified slices from kymographs corresponding to spindle length of 2.5–5.5 µm. The Cut7–GFP kymograph line-scans were retrieved from 1162 frames collected from 29 Cut7–GFP cells, and from 1169 frames collected from 40 Cut7-988–GFP cells. All individual line scans were aligned based on one of the spindle-pole positions (chosen to be the pole with brighter intensity). We then summed all line scans to determine the total Cut7–GFP intensity along the spindle axis.

Track and SPB annotation

Annotations were made directly on the kymograph. We created in-house MATLAB software (available upon request) that allowed a user to interactively draw Cut7 tracks (Figs S2, S5, S8, S13). Some of these tracks were identified as corresponding to spindle-pole-localized Cut7–GFP, whereas other tracks were used for motility analysis. For bipolar spindle kymographs, both spindle poles were identified by areas of highest brightness throughout the kymograph. Two SPB lines were traced over those areas. Clusters of Cut7–GFP moving along spindle MTs were then traced. The nearest SPB was used as a reference for describing poleward or anti-poleward movement; events that showed movement all the way from one pole to the other were excluded from analysis due to ambiguity in identifying the nearest SPB. For monopolar spindle kymographs, the SPB was identified by the area of highest brightness throughout the kymograph, and an SPB line was traced. Clusters of Cut7–GFP moving poleward or antipoleward were then traced.

Track merging and event identification

We started by merging tracks that were deemed to belong to the same global track. For example, if track 2 began within some time interval of track 1 ending, and the start position of track 2 was close to the end position of track 1, then we merged the tracks (Fig. S1). After a phase of merging, we identified a number of tracks with both poleward and anti-poleward motion. The tracks were then analyzed by splitting them into poleward, anti-poleward, and paused segments or events. Event identification was based on the average local velocity along the track. A cutoff value of 3 nm s^{-1} was used to distinguish directed movement from pausing. Points with velocity less than the negative of the cutoff were assigned as poleward, whereas points with velocity greater than the cutoff were assigned as anti-poleward. The remaining points were assigned as paused.

Track analysis quantification

Tracks were analyzed with reference to the position of the SPB. To do that, we assigned each track to its nearest SPB. For monopolar spindles, there was only one pole and assignment was straightforward. For bipolar spindles with two SPBs, we picked the SPB that was closest to the track start position. Tracks that moved all the way across the bipolar spindle from one pole to another were excluded from this analysis. Distance and velocity were measured relative to the closest SPB. For each kymograph, the frequency of directional events was calculated by counting the number of poleward and anti-poleward tracks and dividing by the total time of the kymograph. The switching frequency was calculated by counting the number of switches out of a state (poleward and anti-poleward movement) divided by the total time of all tracks in that state. For example, the switching frequency for exiting the poleward-moving state was calculated by dividing the number of transitions out of the poleward state by the total time of all poleward tracks.

Acknowledgements

We thank Mohan Balasubramanian, Anne Paoletti, Takashi Toda, and Yoshi Wantanabe for gifts of strains used to construct the strains in this study, the National Bio-Resource Project–Yeast, Japan for providing NBRP strains FY23688 and FY31411, along with Pombase and the Wellcome Trust for providing online resources for Cut7 and other fission yeast proteins. We thank Michelle Saini for a generous donation of useful equipment, and acknowledge the Department of Moleculer, Cellular, and Developmental Biology (MCDB) Light Microscopy Core Facility for assistance with live-cell imaging and the Biocore Facility of MCD for use of the Nanodrop 2000.

Competing interests

The authors declare no competing or financial interests.

Author contributions

Conceptualization: Z.R.G., M.D.B.; Methodology: Z.R.G., S.A., M.H.J., B.Z., C.C., R.M., M.D.B.; Software: S.A., B.Z., C.C.; Validation: Z.R.G., S.A., M.H.J.; Formal analysis: Z.R.G., S.A., B.Z., C.C., M.D.B.; Investigation: Z.R.G., S.A., M.H.J.; Resources: Z.R.G., B.Z., C.C., M.D.B.; Data curation: Z.R.G., S.A., M.H.J.; Writing - original draft: Z.R.G., M.H.J., R.M., M.D.B.; Writing - review & editing: Z.R.G., S.A., M.H.J., R.M., M.D.B.; Visualization: Z.R.G., S.A., M.H.J., B.Z., C.C., M.D.B.; Supervision: M.D.B.; Project administration: M.D.B.; Funding acquisition: M.D.B.

Funding

This work was supported by National Institutes of Health (NIH) grant R01 GM124371 and National Science Foundation (NSF) grant DMR 1725065 to M.D.B. Deposited in PMC for release after 12 months.

Data availability

Datasets available at from the CU Boulder PetaLibrary at https://doi.org/10.25810/frzq-3x45.

Peer review history

The peer review history is available online at https://journals.biologists.com/jcs/lookup/doi/10.1242/jcs.260474.reviewer-comments.pdf

References

Acar, S., Carlson, D. B., Budamagunta, M. S., Yarov-Yarovoy, V., Correia, J. J., Niñonuevo, M. R., Jia, W., Tao, L., Leary, J. A., Voss, J. C. et al. (2013). The bipolar assembly domain of the mitotic motor kinesin-5. *Nat. Commun.* **4**, ncomms2348. doi:10.1038/ncomms2348

Akera, T., Goto, Y., Sato, M., Yamamoto, M. and Watanabe, Y. (2015). Mad1 promotes chromosome congression by anchoring a kinesin motor to the kinetochore. *Nat. Cell Biol.* **17**, 1124-1133. doi:10.1038/ncb3219

Avunie-Masala, R., Movshovich, N., Nissenkorn, Y., Gerson-Gurwitz, A., Fridman, V., Kõivomägi, M., Loog, M., Hoyt, M. A., Zaritsky, A. and Gheber, L. (2011). Phospho-regulation of kinesin-5 during anaphase spindle elongation. *J. Cell Sci.* **124**, 873-878. doi:10.1242/jcs.077396

Balchand, S. K., Mann, B. J., Titus, J., Ross, J. L. and Wadsworth, P. (2015). TPX2 inhibits Eg5 by interactions with both motor and microtubule. *J. Biol. Chem.* **290**, 17367-17379. doi:10.1074/jbc.M114.612903

Blackwell, R., Sweezy-Schindler, O., Baldwin, C., Hough, L. E., Glaser, M. A. and Betterton, M. D. (2016). Microscopic origins of anisotropic active stress in motor-driven nematic liquid crystals. *Soft Mat.* **12**, 2676-2687. doi:10.1039/C5SM02506K

Blackwell, R., Sweezy-Schindler, O., Edelmaier, C., Gergely, Z. R., Flynn, P. J., Montes, S., Crapo, A., Doostan, A., Mcintosh, J. R., Glaser, M. A. et al. (2017). Contributions of microtubule dynamic instability and rotational diffusion to kinetochore capture. *Biophys. J.* **112**, 552-563. doi:10.1016/j.bpj.2016.09.006

Blangy, A., Lane, H. A., D'hérin, P., Harper, M., Kress, M. and Niggt, E. A. (1995). Phosphorylation by p34cdc2 regulates spindle association of human Eg5, a kinesin-related motor essential for bipolar spindle formation in vivo. *Cell* **83**, 1159-1169. doi:10.1016/0092-8674(95)90142-6

Bodrug, T., Wilson-Kubalek, E. M., Nithianantham, S., Thompson, A. F., Alfieri, A., Gaska, I., Major, J., Debs, G., Inagaki, S., Gutierrez, P. et al. (2020). The kinesin-5 tail domain directly modulates the mechanochemical cycle of the motor domain for anti-parallel microtubule sliding. *eLife* **9**, e51131. doi:10.7554/eLife.51131

Britto, M., Goulet, A., Rizvi, S., Von Loeffelholz, O., Moores, C. A. and Cross, R. A. (2016). Schizosaccharomyces pombe kinesin-5 switches direction using a steric blocking mechanism. *Proc. Natl Acad. Sci. USA* **113**, E7483-E7489. doi:10.1073/pnas.1611581113

Cahu, J. and Surrey, T. (2009). Motile microtubule crosslinkers require distinct dynamic properties for correct functioning during spindle organization in Xenopus egg extract. *J. Cell Sci.* **122**, 1295-1300. doi:10.1242/jcs.044248

Cahu, J., Olichon, A., Hentrich, C., Schek, H., Drinjakovic, J., Zhang, C., Doherty-Kirby, A., Lajoie, G. and Surrey, T. (2008). Phosphorylation by Cdk1 increases the binding of Eg5 to microtubules in vitro and in Xenopus egg extract spindles. *PLoS ONE* **3**, e3936. doi:10.1371/journal.pone.0003936

Chang, L. and Gould, K. L. (2000). Sid4p is required to localize components of the septation initiation pathway to the spindle pole body in fission yeast. *Proc. Natl Acad. Sci. USA* **97**(10), 5249-5254. doi:10.1073/pnas.97.10.5249

Cole, D. G., Saxton, W. M., Sheehan, K. B. and Scholey, J. M. (1994). A "slow" homotetrameric kinesin-related motor protein purified from Drosophila embryos. *J. Biol. Chem.* **269**, 22913-22916. doi:10.1016/S0021-9258(17)31593-4

Ding, R., Mcdonald, K. L. and Mcintosh, J. R. (1993). Three-dimensional reconstruction and analysis of mitotic spindles from the yeast, Schizosaccharomyces pombe. *J. Cell Biol.* **120**, 141-151. doi:10.1083/jcb.120.1.141

Drummond, D. R. and Hagan, I. M. (1998). Mutations in the bimC box of Cut7 indicate divergence of regulation within the bimC family of kinesin related proteins. *J. Cell Sci.* **111**, 853-865. doi:10.1242/jcs.111.7.853

Düselder, A., Fridman, V., Thiede, C., Wiesbaum, A., Goldstein, A., Klopfenstein, D. R., Zaitseva, O., Janson, M. E., Gheber, L. and Schmidt, C. F. (2015). Deletion of the tail domain of the Kinesin-5 Cin8 affects its directionality. *J. Biol. Chem.* **290**, 16841-16850. doi:10.1074/jbc.M114.620799

Edamatsu, M. (2014). Bidirectional motility of the fission yeast kinesin-5, Cut7. *Biochem. Biophys. Res. Commun.* **446**, 231-234. doi:10.1016/j.bbrc.2014.02.106

Edamatsu, M. (2016). Molecular properties of the N-terminal extension of the fission yeast kinesin-5, Cut7. *Genetics Mol. Res.* **15**, gmr.15017799. doi:10.4238/gmr.15017799

Edelmaier, C., Lamson, A. R., Gergely, Z. R., Ansari, S., Blackwell, R., Mcintosh, J. R., Glaser, M. A. and Betterton, M. D. (2020). Mechanisms of chromosome biorientation and bipolar spindle assembly analyzed by computational modeling. *eLife* **9**, e48787. doi:10.7554/eLife.48787

Enos, A. P. and Morris, N. R. (1990). Mutation of a gene that encodes a kinesin-like protein blocks nuclear division in A. nidulans. *Cell* **60**, 1019-1027. doi:10.1016/0092-8674(90)90350-N

Fridman, V., Gerson-Gurwitz, A., Shapira, O., Movshovich, N., Lakämper, S., Schmidt, C. F. and Gheber, L. (2013). Kinesin-5 Kip1 is a bi-directional motor that stabilizes microtubules and tracks their plus-ends in vivo. *J. Cell Sci.* **126**, 4147-4159. doi:10.1242/jcs.125153

Fu, C., Ward, J. J., Loiodice, I., Velve-Casquillas, G., Nedelec, F. J. and Tran, P. T. (2009). Phospho-regulated interaction between Kinesin-6 Klp9p and microtubule bundler Ase1p promotes spindle elongation. *Dev. Cell* **17**, 257-267. doi:10.1016/j.devcel.2009.06.012

Gable, A., Qiu, M., Titus, J., Balchand, S., Ferenz, N. P., Ma, N., Collins, E. S., Fagerstrom, C., Ross, J. L., Yang, G. et al. (2012). Dynamic reorganization of Eg5 in the mammalian spindle throughout mitosis requires dynein and TPX2. *Mol. Biol. Cell* **23**, 1254-1266. doi:10.1091/mbc.e11-09-0820

Gergely, Z. R., Crapo, A., Hough, L. E., Mcintosh, J. R. and Betterton, M. D. (2016). Kinesin-8 effects on mitotic microtubule dynamics contribute to spindle function in fission yeast. *Mol. Biol. Cell* **27**, 3490-3514. doi:10.1091/mbc.e15-07-0505

Gerson-Gurwitz, A., Thiede, C., Movshovich, N., Fridman, V., Podolskaya, M., Danieli, T., Lakämper, S., Klopfenstein, D. R., Schmidt, C. F. and Gheber, L. (2011). Directionality of individual kinesin-5 Cin8 motors is modulated by loop 8, ionic strength and microtubule geometry: control of Cin8 directionality. *EMBO J.* **30**, 4942. doi:10.1038/emboj.2011.403

Gordon, D. M. and Roof, D. M. (1999). The kinesin-related protein Kip1p of Saccharomyces cerevisiae is bipolar. *J. Biol. Chem.* **274**, 28779-28786. doi:10.1074/jbc.274.40.28779

Goshima, G. and Scholey, J. M. (2010). Control of mitotic spindle length. *Annu. Rev. Cell Dev. Biol.* **26**, 21-57. doi:10.1146/annurev-cellbio-100109-104006

Hagan, I. and Yanagida, M. (1990). Novel potential mitotic motor protein encoded by the fission yeast cut7+ gene. *Nature* **347**, 563-566. doi:10.1038/347563a0

Hagan, I. and Yanagida, M. (1992). Kinesin-related cut 7 protein associates with mitotic and meiotic spindles in fission yeast. *Nature* **356**, 74. doi:10.1038/356074a0

Heck, M. M., Pereira, A., Pesavento, P., Yannoni, Y., Spradling, A. C. and Goldstein, L. S. (1993). The kinesin-like protein KLP61F is essential for mitosis in Drosophila. *J. Cell Biol.* **123**, 665-679. doi:10.1083/jcb.123.3.665

Hildebrandt, E. R., Gheber, L., Kingsbury, T. and Andrew Hoyt, M. (2006). Homotetrameric Form of Cin8p, a Saccharomyces cerevisiae Kinesin-5 Motor, Is Essential for Its in Vivo Function. *J. Biol. Chem.* **281**, 26004-26013. doi:10.1074/jbc.M604817200

Hirano, T., Funahashi, S.-I., Uemura, T. and Yanagida, M. (1986). Isolation and characterization of Schizosaccharomyces pombe cut mutants that block nuclear division but not cytokinesis. *EMBO J.* **5**, 2973-2979. doi:10.1002/j.1460-2075.1986.tb04594.x

Hoyt, M. A., He, L., Loo, K. K. and Saunders, W. S. (1992). Two Saccharomyces cerevisiae kinesin-related gene products required for mitotic spindle assembly. *J. Cell Biol.* **118**, 109-120. doi:10.1083/jcb.118.1.109

Hwang, W., Toda, T. and Yukawa, M. (2022). Complementation of fission yeast kinesin-5/Cut7 with human Eg5 provides a versatile platform for screening of anticancer compounds. *Biosci. Biotechnol. Biochem.* **86**, 254-259. doi:10.1093/bbb/zbab212

Kalinina, I., Nandi, A., Delivani, P., Chacón, M. R., Klemm, A. H., Ramunno-Johnson, D., Krull, A., Lindner, B., Pavin, N. and Tolić-Nørrelykke, I. M. (2012). Pivoting of microtubules around the spindle pole accelerates kinetochore capture. *Nat. Cell Biol.* **15**, 82-87. doi:10.1038/ncb2640

Kapitein, L. C., Peterman, E. J. G., Kwok, B. H., Kim, J. H., Kapoor, T. M. and Schmidt, C. F. (2005). The bipolar mitotic kinesin Eg5 moves on both microtubules that it crosslinks. *Nature* **435**, 114-118. doi:10.1038/nature03503

Kashina, A. S., Baskin, R. J., Cole, D. G., Wedaman, K. P., Saxton, W. M. and Scholey, J. M. (1996). A bipolar kinesin. *Nature* **379**, 270-272. doi:10.1038/379270a0

Kettenbach, A. N., Deng, L., Wu, Y., Baldissard, S., Adamo, M. E., Gerber, S. A. and Moseley, J. B. (2015). Quantitative phosphoproteomics reveals pathways for coordination of cell growth and division by the conserved fission yeast kinase Pom1. *Mol. Cell. Proteomics* **14**, 1275-1287. doi:10.1074/mcp.M114.045245

Koch, A., Krug, K., Pengelley, S., Macek, B. and Hauf, S. (2011). Mitotic substrates of the kinase aurora with roles in chromatin regulation identified through quantitative phosphoproteomics of fission yeast. *Sci. Signal.* **4**, rs6. doi:10.1126/scisignal.2001588

Krüger, L. K., Gélin, M., Ji, L., Kikuti, C., Houdusse, A., Théry, M., Blanchoin, L. and Tran, P. T. (2021). Kinesin-6 Klp9 orchestrates spindle elongation by regulating microtubule sliding and growth. *eLife* **10**, e67489. doi:10.7554/eLife.67489

Lamson, A. R., Moore, J. M., Fang, F., Glaser, M. A., Shelley, M. J. and Betterton, M. D. (2021). Comparison of explicit and mean-field models of cytoskeletal filaments with crosslinking motors. *Eur. Phys. J. E. Soft Matter* **44**, 45. doi:10.1140/epje/s10189-021-00042-9

Lera-Ramirez, M., Nédélec, F. J. and Tran, P. T. (2022). Microtubule rescue at midzone edges promotes overlap stability and prevents spindle collapse during anaphase B. *eLife* **11**, e72630. doi:10.7554/eLife.72630

Lupas, A., Van Dyke, M. and Stock, J. (1991). Predicting coiled coils from protein sequences. *Science* **252**, 1162-1164. doi:10.1126/science.252.5009.1162

Ma, N., Tulu, U. S., Ferenz, N. P., Fagerstrom, C., Wilde, A. and Wadsworth, P. (2010). Poleward transport of TPX2 in the mammalian mitotic spindle requires dynein, Eg5, and microtubule flux. *Mol. Biol. Cell* **21**, 979-988. doi:10.1091/mbc.e09-07-0601

Ma, N., Titus, J., Gable, A., Ross, J. L. and Wadsworth, P. (2011). TPX2 regulates the localization and activity of Eg5 in the mammalian mitotic spindle. *J. Cell Biol.* **195**, 87-98. doi:10.1083/jcb.201106149

Mallavarapu, A., Sawin, K. and Mitchison, T. (1999). A switch in microtubule dynamics at the onset of anaphase B in the mitotic spindle of Schizosaccharomyces pombe. *Curr. Biol.* **9**, 1423-1428. doi:10.1016/S0960-9822(00)80090-1

Mann, B. J. and Wadsworth, P. (2018). Kinesin-5 regulation and function in mitosis. *Trends Cell Biol.* **29**, 66-79. doi:10.1016/j.tcb.2018.08.004

Masuda, H., Sevik, M. and Cande, W. Z. (1992). In vitro microtubule-nucleating activity of spindle pole bodies in fission yeast Schizosaccharomyces pombe: Cell cycle-dependent activation in xenopus cell-free extracts. *J. Cell Biol.* **117**, 1055-1066. doi:10.1083/jcb.117.5.1055

Mayer, T. U., Kapoor, T. M., Haggarty, S. J., King, R. W., Schreiber, S. L. and Mitchison, T. J. (1999). Small molecule inhibitor of mitotic spindle bipolarity identified in a phenotype-based screen. *Science* **286**, 971-974. doi:10.1126/science.286.5441.971

Mcintosh, J. R. and Landis, S. C. (1971). The distribution of spindle microtubules during mitosis in cultured human cells. *J. Cell Biol.* **49**, 468-497. doi:10.1083/jcb.49.2.468

Moreno, S., Klar, A. and Nurse, P. (1991). Molecular genetic analysis of fission yeast Schizosaccharomyces pombe. *In Guide to Yeast Genet. Mol. Biol.* **194**, 795-823. doi:10.1016/0076-6879(91)94059-L

Ohira, M. J., Hendrickson, D. G., McIsaac, R. S. and Rhind, N. (2017). An estradiol-inducible promoter enables fast, graduated control of gene expression in fission yeast. *Yeast* **34**, 323-334. doi:10.1101/092338

Okazaki, K., Okazaki, N., Kume, K., Jinno, S., Tanaka, K. and Okayama, H. (1990). High-frequency transformation method and library transducing vectors for cloning mammalian cDNAs by trans-complementation of Schizosaccharomyces pombe. *Nucleic Acids Res.* **18**, 6485-6489. doi:10.1093/nar/18.22.6485

Olmsted, Z. T., Colliver, A. G., Riehlman, T. D. and Paluh, J. L. (2014). Kinesin-14 and kinesin-5 antagonistically regulate microtubule nucleation by γ-TuRC in yeast and human cells. *Nat. Commun.* **5**, 5339. doi:10.1038/ncomms6339

Pidoux, A. L., Ledizet, M. and Cande, W. Z. (1996). Fission yeast pkl1 is a kinesin-related protein involved in mitotic spindle function. *Mol. Biol. Cell* **7**, 1639-1655. doi:10.1091/mbc.7.10.1639

Rapley, J., Nicolàs, M., Groen, A., Regué, L., Bertran, M. T., Caelles, C., Avruch, J. and Roig, J. (2008). The NIMA-family kinase Nek6 phosphorylates the kinesin Eg5 at a novel site necessary for mitotic spindle formation. *J. Cell Sci.* **121**, 3912-3921. doi:10.1242/jcs.035360

Rincon, S. A., Lamson, A., Blackwell, R., Syrovatkina, V., Fraisier, V., Paoletti, A., Betterton, M. D. and Tran, P. T. (2017). Kinesin-5-independent mitotic spindle assembly requires the antiparallel microtubule crosslinker Ase1 in fission yeast. *Nat. Commun.* **8**, 15286. doi:10.1038/ncomms15286

Rodriguez, A. S., Killilea, A. N., Batac, J., Filopei, J., Simeonov, D., Lin, I. and Paluh, J. L. (2008). Protein complexes at the microtubule organizing center regulate bipolar spindle assembly. *Cell Cycle* **7**, 1246-1253. doi:10.4161/cc.7.9.5808

Roof, D. M., Meluh, P. B. and Rose, M. D. (1992). Kinesin-related proteins required for assembly of the mitotic spindle. *J. Cell Biol.* **118**, 95-108. doi:10.1083/jcb.118.1.95

Roostalu, J., Hentrich, C., Bieling, P., Telley, I. A., Schiebel, E. and Surrey, T. (2011). Directional switching of the kinesin Cin8 through motor coupling. *Science* **332**, 94-99. doi:10.1126/science.1199945

Sagolla, M. J., Uzawa, S. and Cande, W. Z. (2003). Individual microtubule dynamics contribute to the function of mitotic and cytoplasmic arrays in fission yeast. *J. Cell Sci.* **116**, 4891-4903. doi:10.1242/jcs.00796

Sawin, K. E. and Mitchison, T. J. (1995). Mutations in the kinesin-like protein Eg5 disrupting localization to the mitotic spindle. *Proc. Natl Acad. Sci. USA* **92**, 4289-4293. doi:10.1073/pnas.92.10.4289

Sawin, K. E., Leguellec, K., Philippe, M. and Mitchison, T. J. (1992). Mitotic spindle organization by a plus-end-directed microtubule motor. *Nature* **359**, 540-543. doi:10.1038/359540a0

Scholey, J. E., Nithianantham, S., Scholey, J. M. and Al-Bassam, J. (2014). Structural basis for the assembly of the mitotic motor Kinesin-5 into bipolar tetramers. *eLife* **3**, e02217. doi:10.7554/eLife.02217

Scholey, J. M., Civelekoglu-Scholey, G. and Brust-Mascher, I. (2016). Anaphase B. *Biology* **5**, 51. doi:10.3390/biology5040051

Shapira, O. and Gheber, L. (2016). Motile properties of the bi-directional kinesin-5 Cin8 are affected by phosphorylation in its motor domain. *Sci. Rep.* **6**, 25597. doi:10.1038/srep25597

Shapira, O., Goldstein, A., Al-Bassam, J. and Gheber, L. (2017). A potential physiological role for bi-directional motility and motor clustering of mitotic kinesin-5 Cin8 in yeast mitosis. *J. Cell Sci.* **130**, 725-734. doi:10.1242/jcs.195040

Sharp, D. J., Mcdonald, K. L., Brown, H. M., Matthies, H. J., Walczak, C., Vale, R. D., Mitchison, T. J. and Scholey, J. M. (1999). The bipolar kinesin, KLP61F, cross-links microtubules within interpolar microtubule bundles of Drosophila embryonic mitotic spindles. *J. Cell Biol.* **144**, 125-138. doi:10.1083/jcb.144.1.125

Shimamoto, Y., Forth, S. and Kapoor, T. M. (2015). Measuring pushing and braking forces generated by ensembles of kinesin-5 crosslinking two microtubules. *Dev. Cell* **34**, 669-681. doi:10.1016/j.devcel.2015.08.017

Singh, S. K., Pandey, H., Al-Bassam, J. and Gheber, L. (2018). Bidirectional motility of kinesin-5 motor proteins: Structural determinants, cumulative functions and physiological roles. *Cell. Mol. Life Sci.* **75**, 1757-1771. doi:10.1007/s00018-018-2754-7

Snaith, H. A., Anders, A., Samejima, I. and Sawin, K. E. (2010). Chapter 9 - New and old reagents for fluorescent protein tagging of microtubules in fission yeast: experimental and critical evaluation. In Lynne Cassimeris and Phong Tran, editor. *Methods Cell Biol.* **97**, 147-172. doi:10.1016/S0091-679X(10)97009-X

Tallada, V. A., Tanaka, K., Yanagida, M. and Hagan, I. M. (2009). The S. pombe mitotic regulator Cut12 promotes spindle pole body activation and integration into the nuclear envelope. *J. Cell Biol.* **185**, 875-888. doi:10.1083/jcb.200812108

Tao, L., Mogilner, A., Civelekoglu-Scholey, G., Wollman, R., Evans, J., Stahlberg, H. and Scholey, J. M. (2006). A homotetrameric kinesin-5, KLP61F, bundles microtubules and antagonizes Ncd in motility assays. *Curr. Biol.* **16**, 2293-2302. doi:10.1016/j.cub.2006.09.064

Thiede, C., Fridman, V., Gerson-Gurwitz, A., Gheber, L. and Schmidt, C. F. (2012). Regulation of bi-directional movement of single kinesin-5 Cin8 molecules. *BioArchitecture* **2**, 70-74. doi:10.4161/bioa.20395

Troxell, C. L., Sweezy, M. A., West, R. R., Reed, K. D., Carson, B. D., Pidoux, A. L., Cande, W. Z., Mcintosh, J. R. and Stearns, T. (2001). Pkl1+ and klp2+: two kinesins of the Kar3 subfamily in fission yeast perform different functions in both mitosis and meiosis. *Mol. Biol. Cell* **12**, 3476-3488. doi:10.1091/mbc.12.11.3476

Unsworth, A., Masuda, H., Dhut, S. and Toda, T. (2008). Fission yeast kinesin-8 Klp5 and Klp6 are interdependent for mitotic nuclear retention and required for proper microtubule dynamics. *Mol. Biol. Cell* **19**, 5104-5115. doi:10.1091/mbc.e08-02-0224

Uteng, M., Hentrich, C., Miura, K., Bieling, P. and Surrey, T. (2008). Poleward transport of Eg5 by dynein–dynactin in Xenopus laevis egg extract spindles. *J. Cell Biol.* **182**, 715-726. doi:10.1083/jcb.200801125

Van Den Wildenberg, S. M. J. L., Tao, L., Kapitein, L. C., Schmidt, C. F., Scholey, J. M. and Peterman, E. J. G. (2008). The homotetrameric kinesin-5 KLP61F preferentially crosslinks microtubules into antiparallel orientations. *Curr. Biol.* **18**, 1860-1864. doi:10.1016/j.cub.2008.10.026

Ward, J. J., Roque, H., Antony, C. and Nédélec, F. (2015). Mechanical design principles of a mitotic spindle. *eLife* **3**, e03398. doi:10.7554/eLife.03398

Weinger, J. S., Qiu, M., Yang, G. and Kapoor, T. M. (2011). A nonmotor microtubule binding site in kinesin-5 is required for filament crosslinking and sliding. *Curr. Biol.* **21**, 154-160. doi:10.1016/j.cub.2010.12.038

West, R. R., Malmstrom, T., Troxell, C. L. and Mcintosh, J. R. (2001). Two related kinesins, klp5+ and klp6+, foster microtubule disassembly and are required for meiosis in fission yeast. *Mol. Biol. Cell* **12**, 3919-3932. doi:10.1091/mbc.12.12.3919

West, R. R., Vaisberg, E. V., Ding, R., Nurse, P. and Richard Mcintosh, J. (1998). Cut11+: a gene required for cell cycle-dependent spindle pole body anchoring in the nuclear envelope and bipolar spindle formation in Schizosaccharomyces pombe. *Mol. Biol. Cell* **9**, 2839-2855. doi:10.1091/mbc.9.10.2839

Wilson-Grady, J. T., Villén, J. and Gygi, S. P. (2008). Phosphoproteome analysis of fission yeast. *J. Proteome Res.* **7**, 1088-1097. doi:10.1021/pr7006335

Yamagishi, Y., Yang, C. H., Tanno, Y. and Watanabe, Y. (2012). MPS1/Mph1 phosphorylates the kinetochore protein KNL1/Spc7 to recruit SAC components. *Nat. Cell Biol.* **14**, 746-752. doi:10.1038/ncb2515

Yukawa, M., Ikebe, C. and Toda, T. (2015). The Msd1–Wdr8–Pkl1 complex anchors microtubule minus ends to fission yeast spindle pole bodies. *J. Cell Biol.* **209**, 549-562. doi:10.1083/jcb.201412111

Yukawa, M., Yamada, Y., Yamauchi, T. and Toda, T. (2018). Two spatially distinct kinesin-14 proteins, Pkl1 and Klp2, generate collaborative inward forces against kinesin-5 Cut7 in S. pombe. *J. Cell Sci.* **131**, jcs.210740. doi:10.1242/jcs.210740

Yukawa, M., Okazaki, M., Teratani, Y., Furuta, K. and Toda, T. (2019). Kinesin-6 Klp9 plays motor-dependent and -independent roles in collaboration with kinesin-5 Cut7 and the microtubule crosslinker Ase1 in fission yeast. *Sci. Rep.* **9**, 7336. doi:10.1038/s41598-019-43774-7

Yukawa, M., Teratani, Y. and Toda, T. (2020). How essential Kinesin-5 becomes non-essential in fission yeast: force balance and microtubule dynamics matter. *Cells* **9**, 1154. doi:10.3390/cells9051154

Zhang, D. and Oliferenko, S. (2014). Tts1, the fission yeast homologue of the TMEM33 family, functions in NE remodeling during mitosis. *Mol. Biol. Cell* **25**, 2970-2983. doi:10.1091/mbc.e13-12-0729

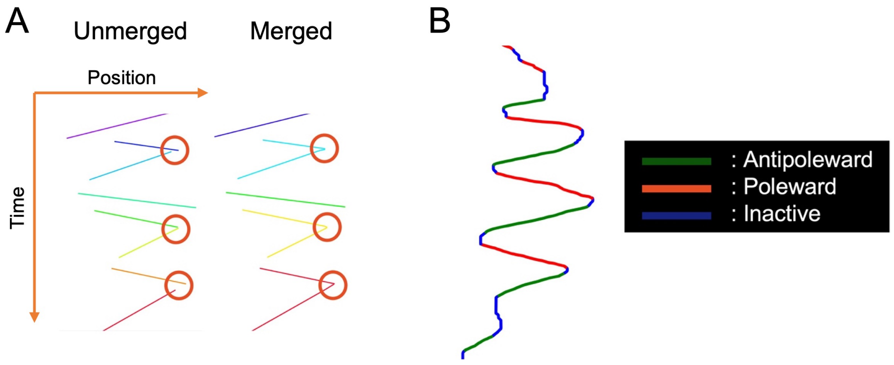

Fig. S1. Schematic of track preprocessing. (A) Track merging. Unmerged tracks (left) and merged tracks (right). The possible merging events are indicated by orange circles. Tracks with ends that are close together in space and time are merged. (B) Tracks are split into poleward (red), antipoleward (green), and inactive (blue) segments based on local velocity. This enables analysis of tracks based on their directional state.

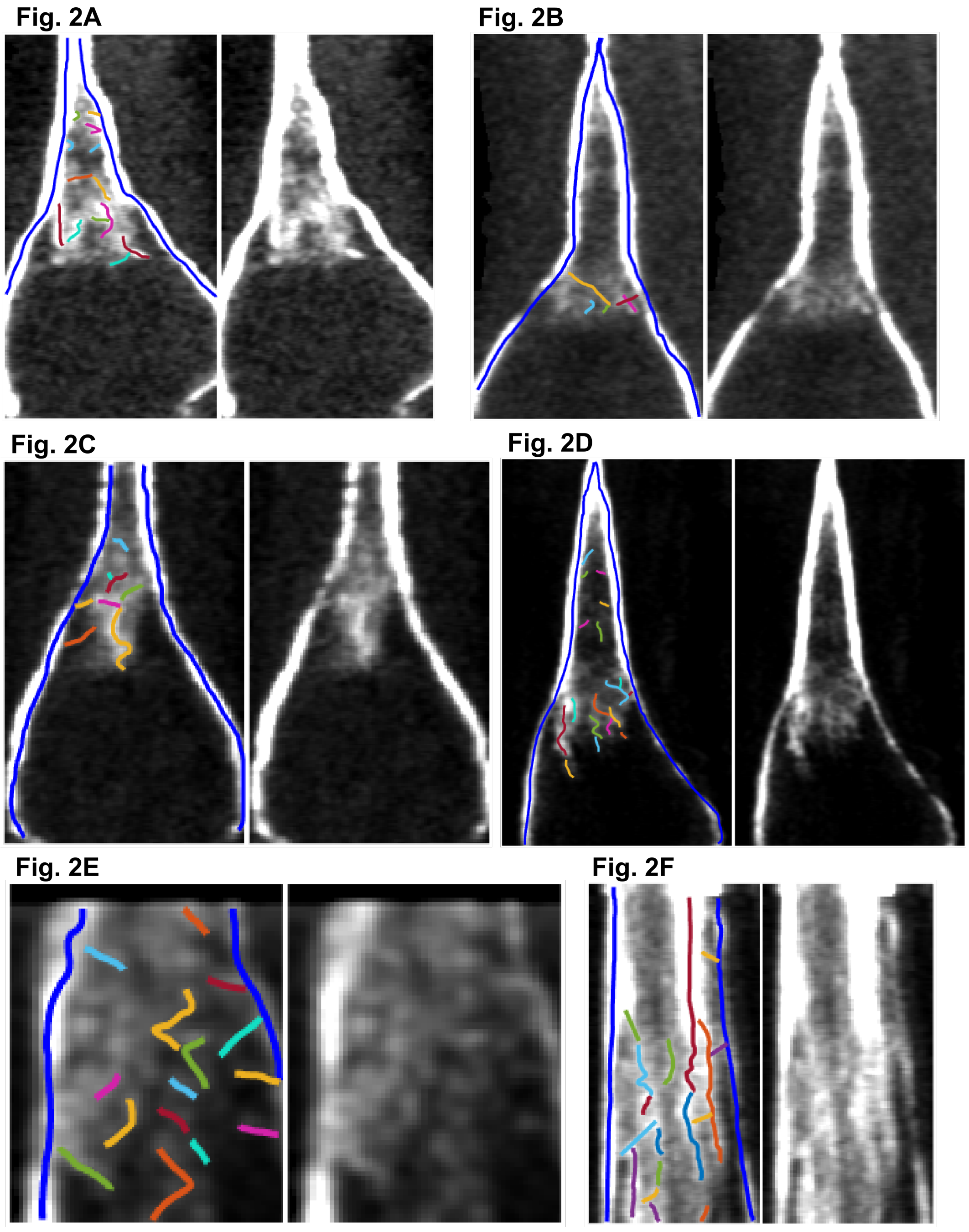

Fig. 2A

Fig. 2B

Fig. 2C

Fig. 2D

Fig. 2E

Fig. 2F

Fig. S2. Overlay of Cut7-GFP kymographs of main text figure 2 with hand-traced Cut7-GFP tracks. Dark blue lines trace the SPBs and other colors trace Cut7-GFP movement.

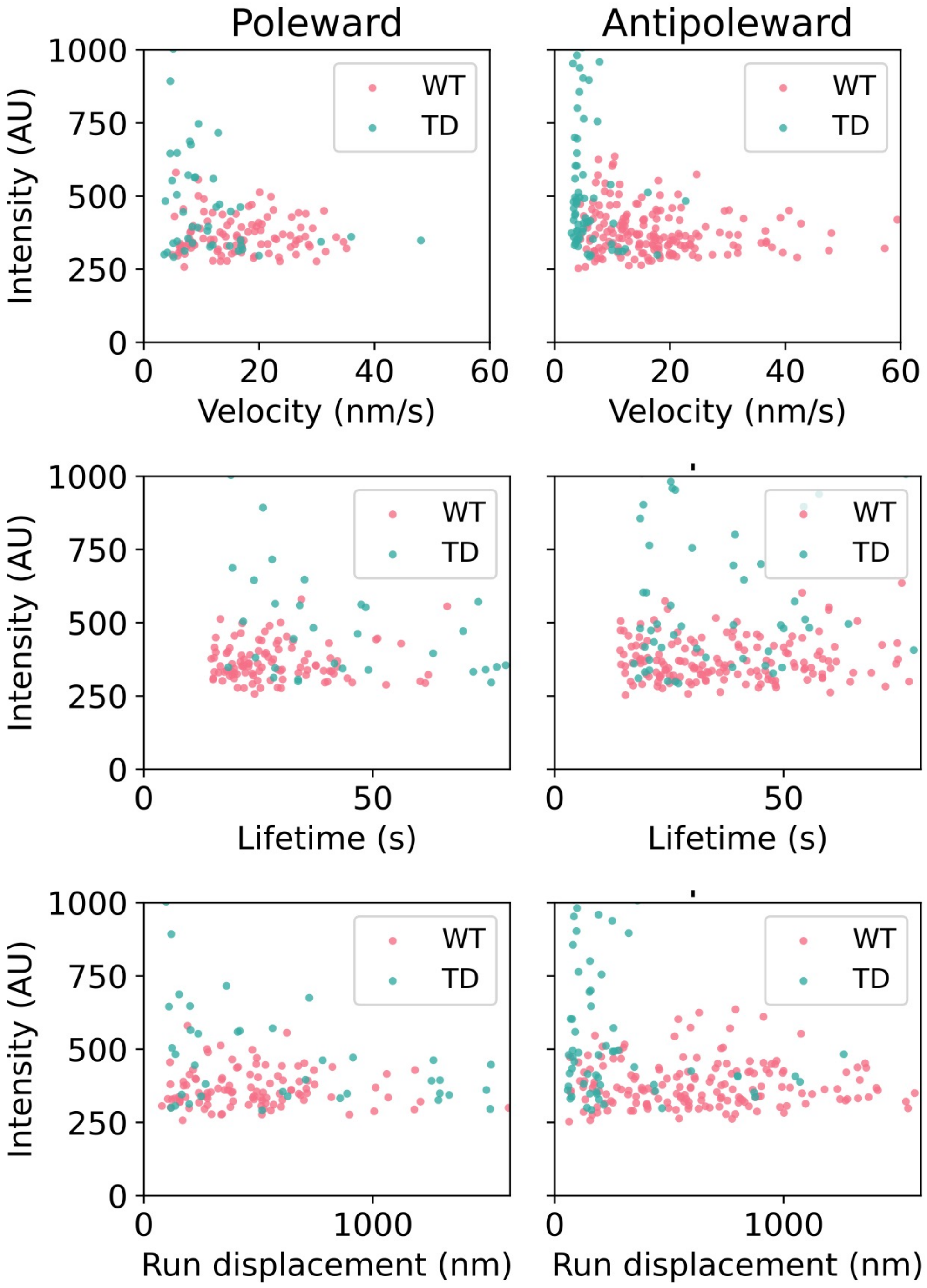

Fig. S3. Scatter plots showing the lack of correlation between velocity and intensity (upper), lifetime and intensity (middle) and run displacement and intensity (lower) for directed events on bipolar spindles of Cut7-GFP (pink) and Cut7-988-GFP (green).

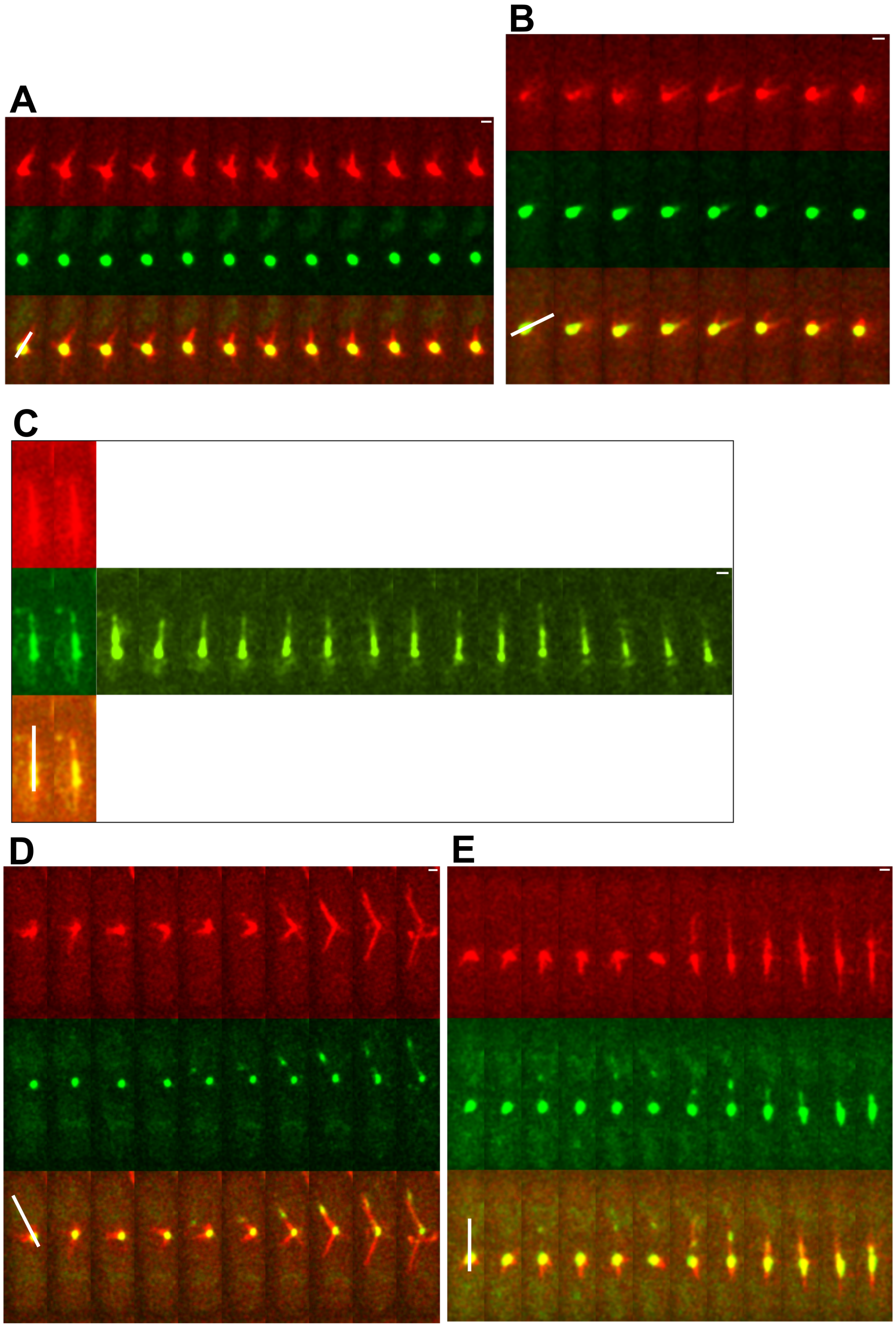

Fig. S4. Two-color images for kymographs shown in figure 3A-E of cut11-7 monopolar spindles at 37^{O}C showing mCherry-atb2 (top, red), Cut7-GFP (middle, green), and merge (lower). White lines show the approximate location of the hand-drawn axis used to construct the Cut7-GFP kymographs for movement along a monopolar spindle MT bundle, after aligning the green channel. Panel C shows a photobleaching experiment in which the red channel was imaged only for two frames prior to bleaching. The mCherry-atb2 fluorescence prior to bleaching was used to identify the MT bundle. Scale bar: 1 μm. Time between images: 27s (A), 24s (B), 23s (C), 60s (D), 60s (E).

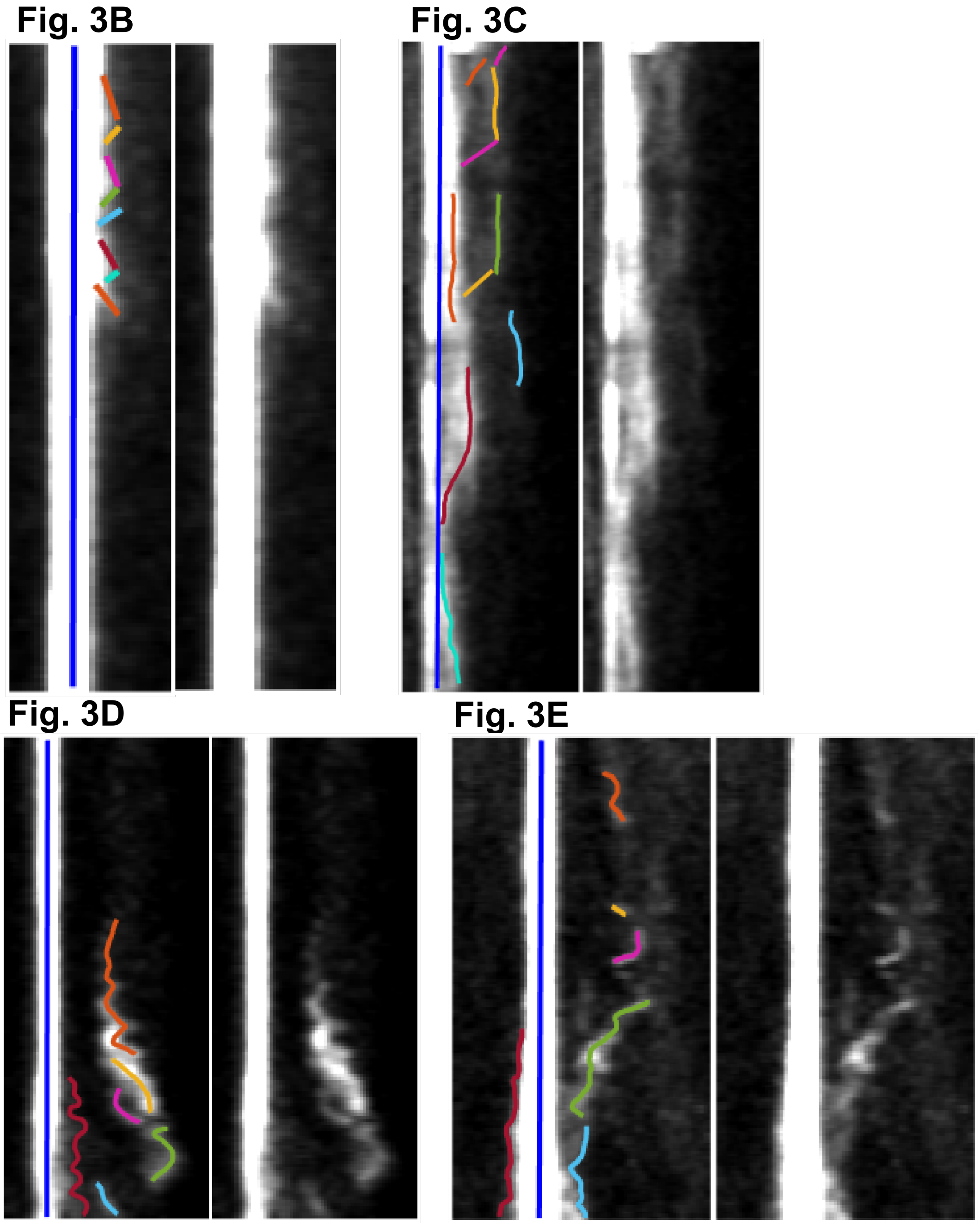

Fig. S5. Overlay of Cut7-GFP kymographs of main text figure 3 with hand-traced Cut7-GFP tracks. Dark blue lines trace the SPBs and other colors trace Cut7-GFP movement.

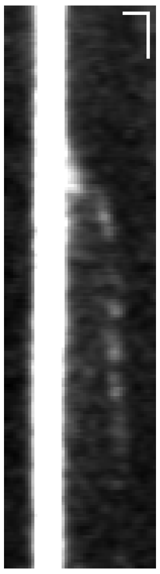

Fig. S6. Kymograph of Cut7-GFP on cut11-7 monopolar spindle showing a distinct, faint track of Cut7-GFP signal that originated near the spindle pole and moved toward microtubule plus ends (anti-poleward). Scale bars, 1 µm and 30 sec.

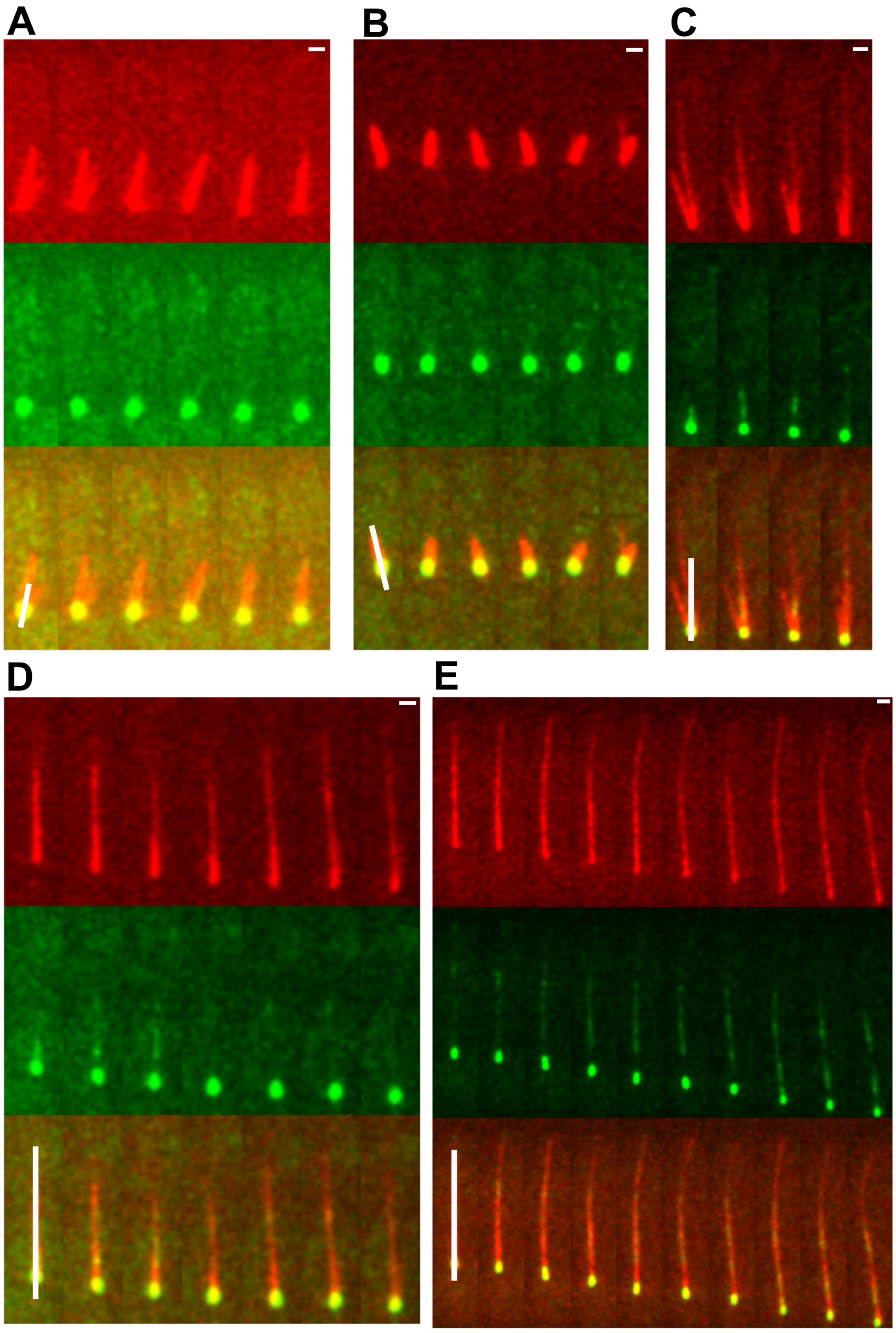

Fig. S7. Two-color images for kykmographs shown in figure 4A-E of cut11-7 klp5Δ monopolar spindles at 37 °C showing mCherry-atb2 (top, red), Cut7-GFP (middle, green), and merge (lower). White lines show the approximate location of the hand-drawn axis used to construct the Cut7-GFP kymographs for movement along a monopolar spindle MT bundle, after aligning the green channel. Scale bar: 1 µm. Time between images: 62s (A), 60s (B), 63s (C), 61s (D), 60s (E).

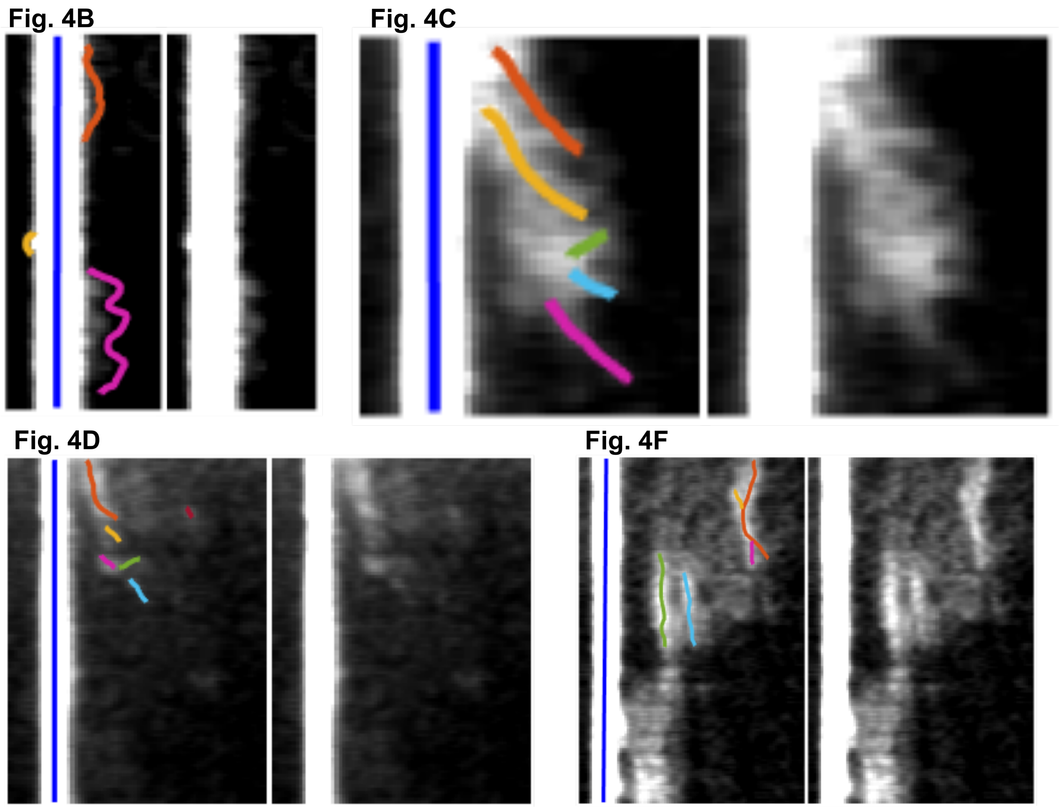

Fig. S8. Overlay of Cut7-GFP kymographs of main text figure 4 with hand-traced Cut7-GFP tracks. Dark blue lines trace the SPBs and other colors trace Cut7-GFP movement.

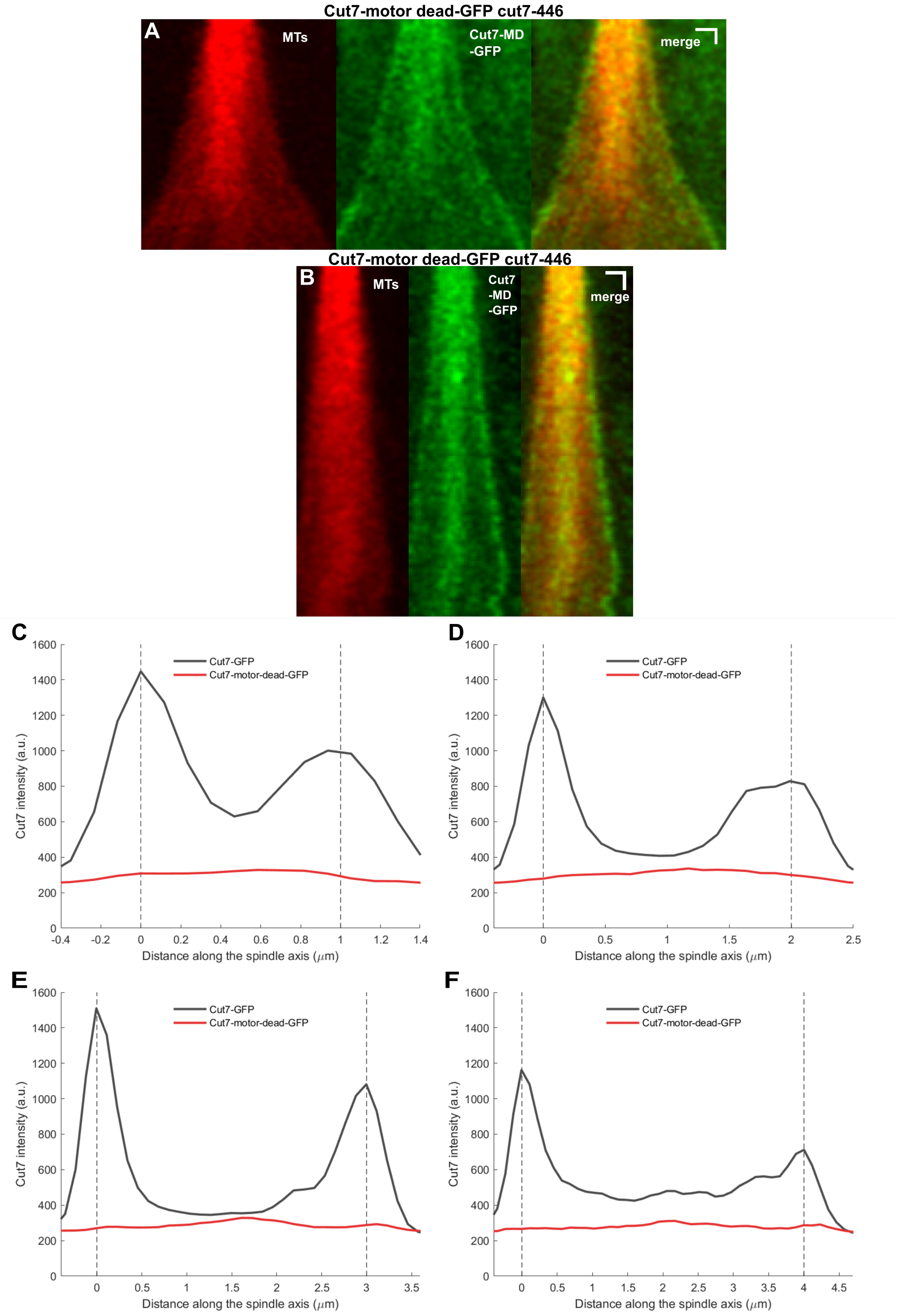

Fig. S9. A,B) Kymographs showing microtubule intensity along the spindle (red, left), Cut7-motor-dead-GFP (green, center), and merge (right). The expression of Cut7-motor-dead-GFP in the cut7-446 background is low, leading to dim fluorescence on spindle microtubules. Therefore, we separately adjusted the brightness and contrast of the red and green channels to make the Cut7-motor-dead-GFP spots visible. Scale bars, 1 μm and 60 sec. C-F: Analysis of Cut7-motor-dead-GFP intensity distribution along the spindle, compared to Cut7-GFP. Cut7-motor-dead-GFP does not show the peaks near spindle poles visible for Cut7-GFP.

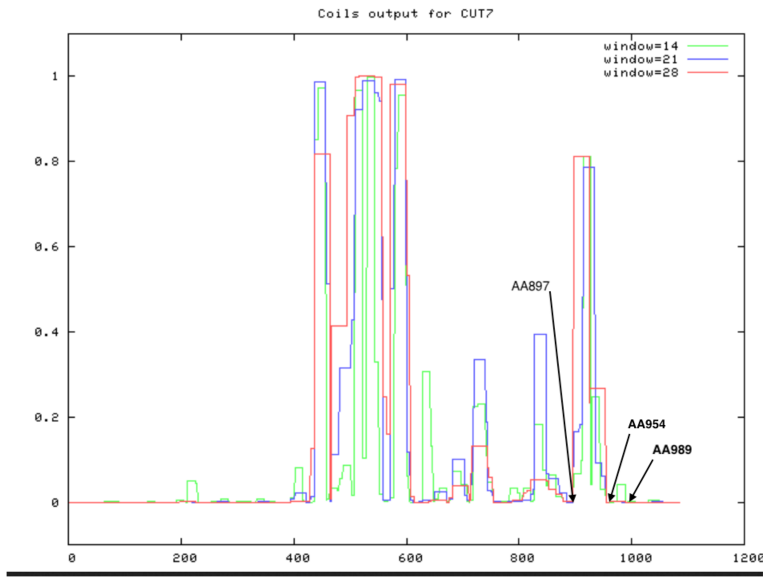

Fig. S10. Coiled-coil prediction for cut7. The likelihood of a coiled coil region is plotted versus cut7+ amino acid number [Lupas et al., 1991]. All 3 prediction windows (green, blue, and red lines) show that the predicted coiled coil region does not extend into the tail beyond amino acid 989. This motivated our construction of the tail-deletion mutant via truncation at amino acid 988.

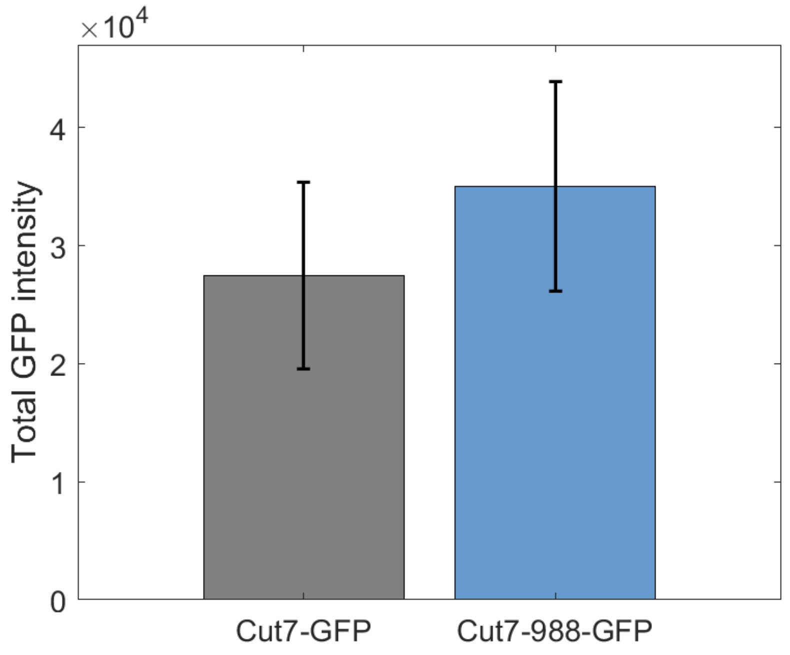

Fig. S11. Comparison of total GFP signal intensity from line-scans along the spindle axis for Cut7-GFP and Cut7-988-GFP. Data were collected from kymographs of spindle length of 2.5-5.5 μm. The Cut7-GFP kymograph line-scans were retrieved from 1162 frames collected from 29 Cut7-GFP cells, and from 1169 frames collected from 40 Cut7-988-GFP cells.

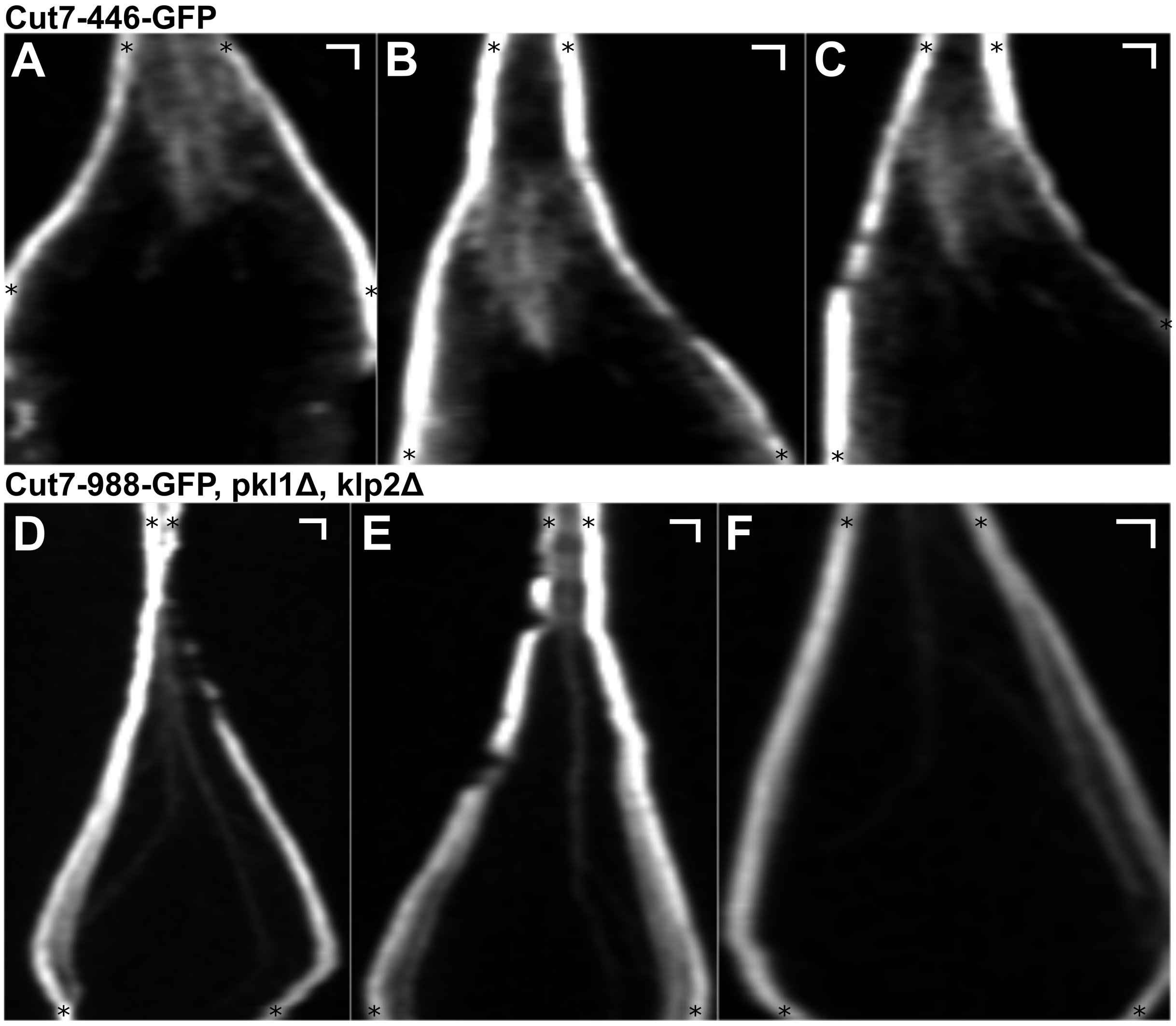

Fig. S12. Brightness- and contrast-matched kymographs corresponding to main text Fig. 5C-E,G-I (A-C) Kymographs of Cut7-446-GFP. (D-F) Kymographs of Cut7-988-GFP. The midzone intensity of Cut7-988-GFP is significantly reduced compared to Cut7-446-GFP. SPBs: asterisks; vertical scale bars: 60 s; horizontal scale bars 1 µm.

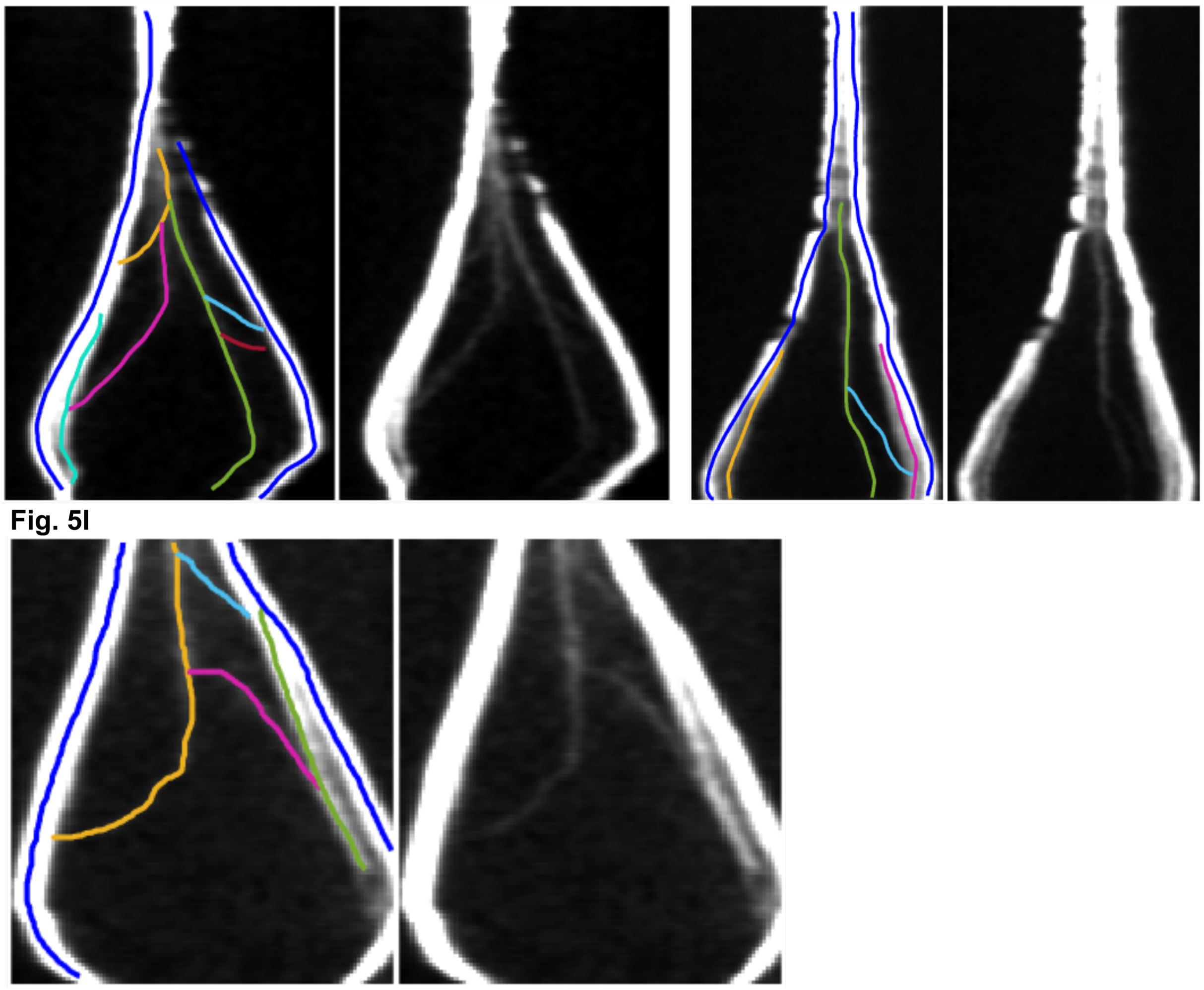

Fig. 5G

Fig. 5H

Fig. 5I

Fig. S13. Overlay of Cut7-GFP kymographs of main text figure 5 with hand-traced Cut7-GFP tracks. Dark blue lines trace the SPBs and other colors trace Cut7-GFP movement.

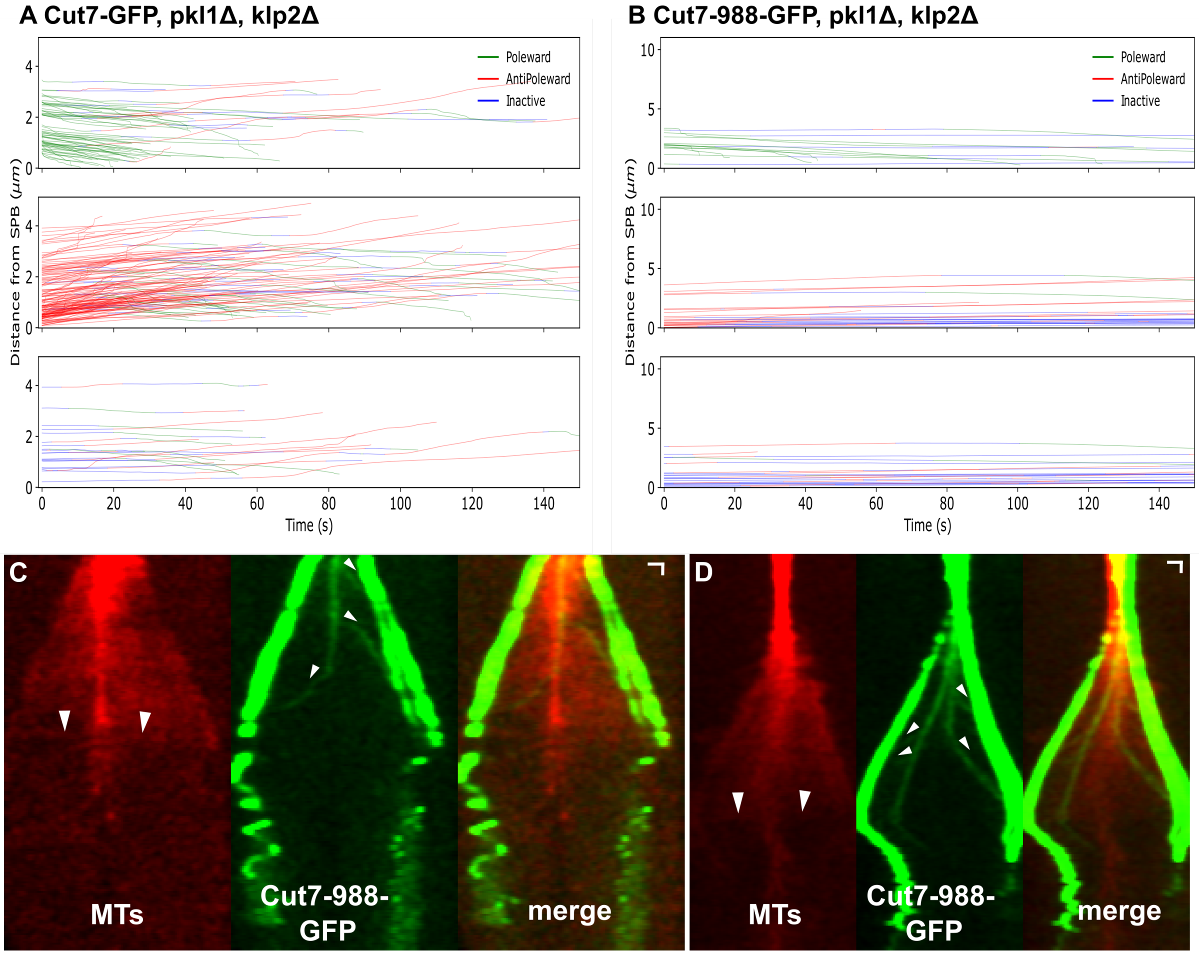

Fig. S14. Comparison of track analysis for (A) Cut7-GFP and (B) Cut7-988-GFP movement on bipolar spindles.(A) Cut7-GFP and (B) Cut7-988-GFP in the pkl1Δ, klp2Δ background. Track segments are colored red for poleward movement, green for anti-poleward movement, and blue for pauses. Top panel, tracks with initial poleward motion. Middle, tracks with initial anti-poleward motion. Bottom, tracks with initial pauses. Movement of Cut7-988-GFP is slower on average, visible as flatter curves in (B) compared to (A). (C) Example kymographs showing microtubules (red) and Cut7-988-GFP (green) on bipolar spindles. The point in time where the red signal decreases at the midzone (labeled by the arrowheads on the red images) indicates the depolymerization of the final anaphase B interpolar MTs. This time is later than the initiation of poleward movement of Cut7-988-GFP (arrowheads on green images). Scale bars, 1μm and 60 sec.

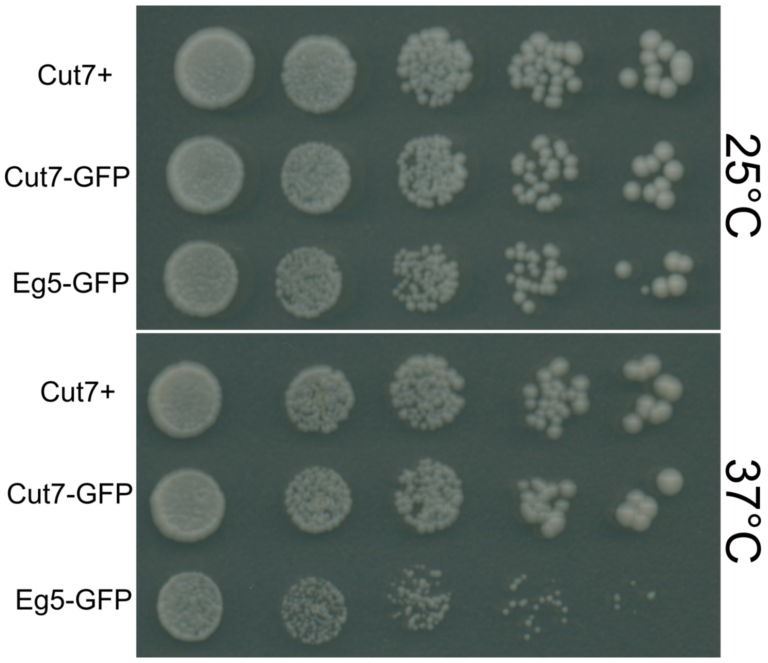

Fig. S15. Growth plates of fission-yeast cells containing cut^{7+}, cut7-GFP, or Eg5-GFP, growing at the indicated temperature. Columns are serial five-fold dilutions. Eg5 complements Cut7p for cell growth at 25 °C, but growth is temperature-sensitive at 37 °C.

Table S1. Quantification of fraction of cells showing visible Cut7 movement, rate of poleward moving events, rate of anti-poleward moving events, switching rate from poleward movements, and switching rate from anti-poleward movements across experimental conditions presented in the main text. For the fraction movement, proportions were compared between genotypes/conditions (rows in the column) with proportions < 1 by the χ^2 test. Most pairs were not statistically significantly different ($p < 0.01$) except as noted: bipolar pre-anaphase B and *klp5*Δ monopolar pre-anaphase B have $p = 0.0033$, bipolar anaphase B and monopolar pre-anaphase B have p = 0.0059, monopolar pre-anaphase B and monopolar anaphase B have $p = 0.0018$, monopolar pre-anaphase B and *klp5*Δ anaphase B have $p = 2.7 \times 10^{-5}$, monopolar anaphase B and klp5Δ pre-anaphase B have $p = 1.8 \times 10^{-4}$. For event and exti rates, the measured quantity in each column was compared across genotypes/conditions (rows in the column) using Student's t-test. All quantities were statistically significantly different with $p < 10^{-4}$ except as noted: AP event rate, bipolar anaphase B (row 2) and monopolar pre-anaphase B (row 3) have $p = 8.1 \times 10^{-4}$, *klp5*Δ pre-anaphase B (row 5) and bipolar Cut7-GFP (row 7) have $p = 0.0043$; P exit rate, bipolar pre-anaphase B (row 1) and monopolar pre-anaphase B (row 3) have $p = 0.0026$, bipolar pre-anaphase B (row 1) and klp5Δ pre-anaphase B have $p = 2.5 \times 10^{-4}$, bipolar anaphase B (row 3) and monopolar pre-anaphase B (row 3) have $p = 0.0021$, monopolar pre-anaphase B (row 3) and klp5Δ pre-anaphase B (row 5) have $p = 0.12$, monopolar pre-anaphase B (row 3) klp5Δ anaphase B (row 6) have $p = 2.6 \times 10^{-4}$, *klp5*Δ pre-anaphase B (row 5) and bipolar Cut7-GFP (row 7) have $p = 0.029$; AP exit rate, bipolar anaphase B (row 2) and bipolar Cut7-GFP (row 7) have $p = 4.4 \times 10^{-4}$, monopolar pre-anaphase B (row 3) and monopolar anaphase B (row 4) have $p = 0.85$, monopolar pre-anaphase B (row 3) and *klp5*Δ pre-anaphase B (row 5) have $p = 0.62$, monopolar anaphase B (row 4) and *klp5*Δ pre-anaphase B (row 5) have $p = 0.10$.

Condition	Fraction movement	P event rate ($\times 10^{-3}$ s^{-1})	AP event rate ($\times 10^{-3}$ s^{-1})	P exit rate ($\times 10^{-3}$ s^{-1})	AP exit rate ($\times 10^{-3}$ s^{-1})
Bipolar pre-anaphase B	0.69 (N=29)	1.8 ± 0.3 (N=36)	3.3 ± 0.4 (N=66)	5.9 ± 2.6 (N=5)	9.7 ± 2.3 (N=18)
Bipolar anaphase B	0.75 (N=27)	6.8 ± 0.6 (N=115)	9.0 ± 0.7 (N=153)	20.5 ± 2.8 (N=52)	12.7 ± 1.4 (N=79)
Monopolar pre-anaphase B	0.31 (N=16)	11.1 ± 2.6 (N=18)	9.9 ± 2.5 (N=16)	26.3 ± 10.7 (N=6)	36.4 ± 12.9 (N=8)
Monopolar anaphase B	0.76 (N=41)	16.6 ± 1.3 (N=166)	19.9 ± 1.4 (N=199)	38.9 ± 4.1 (N=92)	36.7 ± 3.3 (N=123)
Klp5Δ monopolar pre-anaphase B	0.30 (N=27)	4.6 ± 1.0 (N=23)	5.2 ± 1.0 (N=26)	19.7 ± 6.0 (N=11)	38.3 ± 7.8 (N=24)
Klp5Δ monopolar anaphase B	0.91 (N=31)	12.3 ± 0.9 (N=169)	17.9 ± 1.1 (N=246)	32.3 ± 3.1 (N=107)	18.0 ± 1.5 (N=148)
Bipolar Cut7-GFP	1 (N=36)	3.9 ± 0.3 (N=149)	5.5 ± 0.4 (N=209)	17.4 ± 2.3 (N=59)	12.0 ± 1.2 (N=98)
Bipolar Cut7-988-GFP	1 (N=17)	3.2 ± 0.4 (N=67)	6.5 ± 0.6 (N=137)	10.8 ± 1.8 (N=35)	19.0 ± 1.7 (N=123)

Table S2. Quantification of motility parameters of directed Cut7 movement events across experimental conditions pre-sented in the main text. The measured quantity in each column was compared across genotypes/conditions (rows in the column) using Student's t-test. All quantities were statistically significantly different with $p < 10^{-4}$ except as noted: P velocity, bipolar pre-anaphase B (row 1) and and monopolar pre-anaphase B (row 3) have p = 0.68, bipolar anaphase B (row 2) and monopolar pre-anaphase B (row 3) have p = 0.017, monopolar pre-anaphase B (row 3) and monopolar anaphase B (row 4) have p = 0.015, monopolar pre-anaphase B (row 3) and *klp5*Δ pre-anaphase B (row 5) have p = 0.024, monopolar pre-anaphase B (row 3) and bipolar Cut7-GFP have p = 0.041, *klp5*Δ pre-anaphase B (row 5) and *klp5*Δ anaphase (row 6) have p = 0.10; AP velocity, bipolar pre-anaphase B (row 1) and monopolar anaphase B (row 4) have p = 0.18, *klp5*Δ pre-anaphase B (row 5) and anaphase B (row 6) have p = 0.011; P lifetime, Bipolar pre-anaphase B (row 1) and bipolar anaphase B (row 2) have p = 0.036, and bipolar pre-anaphase B (row 1) and *klp5*Δ pre-anaphase B (row 5) have p = 0.013; P lifetime, bipolar pre-anaphase B (row 1) and bipolar anaphase B (row 2) have p = 0.036, bipolar anaphase B (row 2) and bipolar Cut7-GFP (row 7) have p = 0.0021, *klp5*Δ pre-anaphase B (row 5) and bipolar Cut7-GFP (row 7) have p = 0.045; AP lifetime, bipolar pre-anaphase B (row 1) and bipolar Cut7-988-GFP (row 8) have p = 0.02, Bipolar anaphase B (row 2) and bipolar Cut7-988-GFP (row 8) have p = 0.099, bipolar Cut7-GFP (row 7) and bipolar Cut7-988-GFP (row 8) have p = 0.73; P run displacement, Bipolar pre-anaphase (row 1) and bipolar Cut7-988-GFP (row 8) have p = 0.11, Bipolar anaphase B (row 2) and monopolar pre-anaphase B (row 3) have p = 4.7 × 10−4, bipolar anaphase B (row 2) and klp5Δ pre-anaphase B have p = 0.004; AP run displacement, Bipolar pre-anaphase B (row 1) and bipolar anaphase B (row 2) have p = 0.56, bipolar pre-anaphase B (row 1) and bipolar Cut7-GFP have p = 0.42; bipolar anaphase B (row 2) and bipolar Cut7-GFP (row 7) have p = 0.026, monopolar anaphase B (row 4) and klp5Δ anaphase B (row 6) have p = 0.0058.

Condition	P velocity (nm s^{-1})	AP velocity (nm s^{-1})	P lifetime (s)	AP lifetime (s)	P run displacement (nm)	AP run displacement (nm)	P SPB distance (nm)	AP SPB distance (nm)
Bipolar pre-anaphase B	17.6 ± 1.5 (N=26)	20.4 ± 1.9 (N=48)	24.4 ± 2.3 (N=26)	31.7 ± 2.1 (N=48)	505 ± 36 (N=26)	635 ± 61 (N=48)	797 ± 33 (N=110)	875 ± 33 (N=232)
Bipolar anaphase B	15.2 ± 1.1 (N=79)	14.4 ± 0.9 (N=132)	25.2 ± 1.4 (N=79)	39.0 ± 2.5 (N=132)	378 ± 33 (N=79)	630 ± 46 (N=132)	1913 ± 39 (N=348)	1937 ± 33 (N=867)
Monopolar pre-anaphase B	18.6 ± 12.4 (N=17)	36.4 ± 8.0 (N=15)	11.8 ± 2.0 (N=17)	11.3 ± 2.5 (N=15)	342 ± 53 (N=17)	371 ± 73 (N=15)	1112 ± 58 (N=89)	1002 ± 42 (N=107)
Monopolar anaphase B	21.6 ± 2.9 (N=146)	20.9 ± 2.4 (N=184)	13.7 ± 0.8 (N=146)	14.7 ± 1.0 (N=184)	266 ± 29 (N=146)	304 ± 24 (N=184)	1083 ± 41 (N=1168)	1181 ± 34 (N=1730)
Klp5Δ monopolar pre-anaphase B	11.4 ± 1.7 (N=17)	9.8 ± 1.7 (N=23)	26.7 ± 3.5 (N=17)	23.4 ± 1.9 (N=23)	352 ± 33 (N=17)	274 ± 37 (N=23)	818 ± 37 (N=79)	760 ± 26 (N=100)
Klp5Δ monopolar anaphase B	10.9 ± 1.1 (N=127)	10.2 ± 0.5 (N=210)	20.7 ± 1.1 (N=127)	28.8 ± 2.6 (N=210)	237 ± 20 (N=127)	312 ± 32 (N=210)	1637 ± 85 (N=605)	2120 ± 58 (N=1599)
Bipolar Cut7-GFP	16.1 ± 0.9 (N=104)	15.4 ± 0.8 (N=177)	25.8 ± 1.2 (N=104)	37.2 ± 2.1 (N=177)	466 ± 27 (N=104)	641 ± 40 (N=177)	1514 ± 36 (N=456)	1644 ± 30 (N=1111)
Bipolar Cut7-988-GFP	8.6 ± 1.3 (N=46)	4.3 ± 0.4 (N=76)	47.1 ± 6.7 (N=46)	36.8 ± 14.9 (N=76)	540 ± 107 (N=46)	181 ± 162 (N=76)	1721 ± 106 (N=374)	2138 ± 85 (N=727)

Table S3. Comparison of Cut7 motor velocity to MT polymerization and depolymerization velocity.

Condition	Poleward motor/ MT growth velocity (nm s^{-1})	Anti-poleward motor/ MT shrinkage velocity (nm s^{-1})	Reference
Bipolar pre-anaphase B	17.6 ± 1.5	20.4 ± 1.9	Fig. 2
Bipolar anaphase B	15.2 ± 1.1	14.4 ± 0.9	Fig. 2
Monopolar pre-anaphase B	18.6 ± 12.4	36.4 ± 8.0	Fig. 3
Monopolar anaphase B	21.6 ± 2.9	20.9 ± 2.4	Fig. 3
Klp5Δ monopolar pre-anaphase B	11.4 ± 1.7	9.8 ± 1.7	Fig. 4
Klp5Δ monopolar anaphase B	10.9 ± 1.1	10.2 ± 0.5	Fig. 4
Bipolar Cut7-GFP	16.1 ± 0.9	15.4 ± 0.8	Fig. 5
Bipolar Cut7-988-GFP	8.6 ± 1.3	4.3 ± 0.4	Fig. 5
Bipolar anaphase MTs	23	68	Lera-Ramirez et al. [2022]
Monopolar slow MTs	45 ± 15	63.3 ± 35	Kalinina et al. [2012]
Monopolar fast MTs	68.3 ± 25	111.7 ± 23	Blackwell et al. [2017]

Table S4. S. pombe strains used in this work

Strains used in this study		
Note: strains where auxotrophy is not listed are either prototrophs or not determined.		
Strain #	**Description**	**Source**
McI230	pkl1D::his3+, ade6-m210, his3-D1, leu1-32, h+	R McIntosh
McI232	pkl1D::his3+, klp2D::ura4+, ade6-m216, his3-D1, ura4-D18,leu1-32, h+	R McIntosh
MB729	z:adh15:mCherry-atb2:natMX6, leu1-32, ura4-D18, h- (gift of Yoshi Wantanabi)	Y Wantanabi
MB914	cut11-7, z:adh15:mCherry-atb2:natMX6, leu1-32, ura4-D18, h-	this study
MB915	cut11-7, z:adh15:mCherry-atb2:natMX6, leu1-32, ura4-D18, h+	this study
MB921	cut7-446, z:adh15:mCherry-atb2:natMX6, leu1-32, h-	this study
MB929	cut7-3GFP:Kanr, ade6-M210, leu1-32, ura4-D18, h-	P Tran
MB951	cut11-7, z:adh15:mCherry-atb2:natMX6, cut7-3GFP:kanr, leu1-32, ura4-D18, h+	this study
MB953	cut11-7, z:adh15:mCherry-atb2:natMX6, cut7-3GFP:kanr, leu1-32, ura4-D18, h-	this study
MB987	sid4-mCherry:hphMX6, leu1-, ura4-, ade6-, h+	A Paoletti
MB1030	cut11-7, cut7-3GFP:kanr, sid4-mCherry:hphMX6, leu1-32, ura4-D18, h+	this study
MB1032	cut7-3GFP:kanr, sid4-mCherry:hphMX6, leu1-32, ura4-D18, h-	this study
MB1039	cut7-3GFP:kanr, z:adh15:mCherry-atb2:natMX6, leu1-32, ura4-D18, h+	this study
MB1055	kanmx-nmt1-csc1-GFP::ura4+, cdc7mCherry::kanMX, ura-, h+	M Balasubramanian
MB1062	cut11-7, cut7-3GFP:Kanr, cdc7-mcherry:kanr, leu-,ura-, h-	this study
MB1064	cut7-3GFP:Kanr, cdc7-mcherry:kanr, leu-,ura-, h+	this study
MB1068	natR-pkl1-mCherry-hphR, leu1-, ura4-, h-	T Toda
MB1073	pku80::hphMX6, ura-, his2-, h+	YGRC
MB1077	natR-pkl1-mCherry-hphR, cut7-3GFP, leu1-, ura4-, h+	this study
MB1079	cut11-7, natR-pkl1-mCherry-hphR, cut7-3GFP, leu1-, ura4-, h-	this study
MB1081	cut7-Photoactivatable GFP (PA-GFP) -kanr, pku80::hphMX6, ura-, his2-, h+	this study
MB1083	cut7-GFP-kanr, pku80::hphMX6, ura-, his2-, h+	this study
MB1084	pku80::hphMX6, z:adh15:mCherry-atb2:natMX6, ura-, leu-, his2+, h-	this study
MB1085	cut7-PA-GFP-kanr, z:adh15:mCherry-atb2:natMX6, leu-, ura-, h+	this study
MB1088	cut7-PA-GFP-kanr, cut11-7, z:adh15:mCherry-atb2:natMX6, leu-, ura-, h+	this study
MB1093	cut7-446-GFP-kanr, z:adh15:mCherry-atb2:natMX6, leu1-32, h-	this study
MB1098	z:adh15:mCherry-atb2:natMX6, leu1-32, his3-, ura4-, h-	this study
MB1109	pkl1D::his3+, z:adh15:mCherry-atb2:natMX6, his3-, leu1-, h-	this study
MB1112	pkl1D::his3+, cut7-988-tail delete-GFP:kanR, his3-, leu1-, h+	this study
MB1118	pkl1D::his3+, cut7-988-tail delete-GFP:kanR, z:adh15:mCherry-atb2:natMX6, his3-, leu1-, h+	this study
MB1123	pkl1D::his3+, cut7-988-tail delete-GFP:kanR, z:adh15:mCherry-atb2:natMX6, his3-, leu1-, ura4-, h+	this study
MB1131	pkl1D::his3+, klp2::ura4+, cut7-988-tail delete-GFP:kanR, z:adh15:mCherry-atb2:natMX6, his3-, leu1-, ura4-, h?	this study

References

Robert Blackwell, Oliver Sweezy-Schindler, Christopher Edelmaier, Zachary R. Gergely, Patrick J. Flynn, Salvador Montes, Ammon Crapo, Alireza Doostan, J. Richard McIntosh, Matthew A. Glaser, and Meredith D. Betterton. Contributions of Microtubule Dynamic Instability and Rotational Diffusion to Kinetochore Capture. *Biophysical Journal*, 112(3):552–563, February 2017.

Iana Kalinina, Amitabha Nandi, Petrina Delivani, Mariola R. Chacón, Anna H. Klemm, Damien Ramunno-Johnson, Alexander Krull, Benjamin Lindner, Nenad Pavin, and Iva M. Tolić-Norrelykke. Pivoting of microtubules around the spindle pole accelerates kinetochore capture. *Nature Cell Biology*, 2012.

Manuel Lera-Ramirez, François J Nédélec, and Phong T Tran. Microtubule rescue at midzone edges promotes overlap stability and prevents spindle collapse during anaphase B. *eLife*, 11:e72630, March 2022.

Andrei Lupas, Marc Van Dyke, and Jeff Stock. Predicting Coiled Coils from Protein Sequences. *Science*, 252(5009):1162–1164, May 1991.